

## Infiltration into an Analog Fracture: Experimental Observations of Gravity-Driven Fingering

M. J. Nicholl\* and R. J. Glass

### ABSTRACT

The infiltration of water into unsaturated geologic media is an immiscible displacement process that is unstable with respect to gravity and can thus lead to the formation of gravity-driven fingers. Where the geologic media (e.g., rock, soil) is fractured, gravity-driven fingers within the fractures may lead to extremely rapid vertical migration of waterborne contaminants. We designed analog fractures to facilitate the competition between viscous, gravity, and capillary forces that is expected to control finger behavior, then conducted an extended experimental investigation to observe and measure finger behavior. Results show that the spatially variant two-dimensional nature of fracture geometry leads to different behavior than is reported for the related problem of gravity-driven fingers in porous media. Observations of finger behavior are presented, along with a simple scale analysis used to relate the key measures of finger velocity, finger width, and fingertip length. We also present a series of illustrative experiments designed to guide future research.

INFILTRATION is an immiscible displacement process in which water seeps downward into unsaturated soil or rock, displacing the resident air phase from pores and fractures. Simple linear stability theory suggests that gravity will act to destabilize infiltration, while viscous and capillary forces will provide a stabilizing influence (e.g., Saffman and Taylor, 1958; Chouke et al., 1959). Gravity-driven fingers will form in situations where infiltration is unstable. The occurrence and subsequent behavior of gravity-driven fingers in granular porous media (i.e., sands of various textures) has received considerable attention (see reviews in Chen et al., 1995; Chen and Neuman, 1996; Glass and Nicholl, 1996; Scanlon et al., 1997; de Rooij, 2000; Eliassi and Glass, 2002). Conversely, few investigations have considered gravity-driven fingers within individual fractures (Nicholl et al., 1992, 1993a, 1993b, 1994; Glass and Nicholl, 1996; Su et al., 1999, 2001, 2004). Gravity-driven fingers can also occur in free-surface flows on large aperture fractures (e.g., Benson, 2001); however, we restrict our discussion to those that locally saturate the fracture aperture.

The need to consider gravity-driven fingers in fractures as separate from those formed in granular porous media rises from the basic differences in topology of the void spaces between the two. Fracture void space differs from that found in granular porous media in terms of dimensionality (two vs. three), connection, size, isotropy,

and homogeneity. In turn, those differences fundamentally alter the balance between capillary, gravity, and viscous forces that controls the occurrence and behavior of gravity-driven fingers. The two-dimensional nature of fractures forces infiltration to occur at an arbitrary angle with respect to gravity and places constraints on accessibility that lead to greatly enhanced phase entrapment over porous media. Finally, granular porous media commonly exhibits micro-rough grain surfaces and closely spaced intergranular contacts. In fractures, contact points are likely to be widely spaced with respect to the fracture aperture, and in many instances fracture surfaces will be locally smooth. These differences will affect both capillary properties along the air–water interface and the nature of residual moisture content following gravity drainage.

The occurrence of gravity-driven fingers will have a substantial influence on infiltration within an individual fracture. For a given infiltration event, fingers will move much faster and further than would be predicted for a flat (stable) displacement front. In addition, fingers will occupy a much smaller cross-sectional area than a flat front, making them difficult to detect and greatly restricting contact between infiltrating water and the fracture walls. This latter characteristic is critical, as imbibition of water into the adjacent rock matrix and film flow along the fracture walls would slow or perhaps halt advancement within the fracture. Contact with the fracture walls also facilitates processes that inhibit the migration of waterborne contaminants, such as adsorption and chemical or biological degradation. Thus, for infiltration into otherwise low permeability units such as that shown in Fig. 1, the formation of gravity-driven fingers in fractures may lead to transport velocities that are orders of magnitude more rapid than would be expected for capillary (i.e., matrix) dominated flow. Gravity-driven fingers may also be a more ubiquitous occurrence in fractures than in natural porous media, where the presence of fine materials and initial moisture content can act to suppress fingering.

Here, we present laboratory experiments designed to explore gravity-driven fingers formed during infiltration into single fractures. Insight from related areas (Background and Theoretical Network) was used to develop a systematic investigative approach. The experimental design and analog fracture used to control the balance between viscous, capillary, and gravitational forces are presented in Experimental Design. Our results begin with experimental observations of fingers formed during the redistribution of flow that occurs after ponded infiltration (Experimental Observations: Multiple Fingers as Generated via Redistribution Following Ponding Events).

**Abbreviations:** DNAPLS, dense nonaqueous phase liquids.

M.J. Nicholl, Geoscience Dep., Univ. of Nevada, Las Vegas, NV 89122-4010; R.J. Glass, Flow Visualization and Processes Lab., Sandia National Laboratories, Albuquerque, NM. Received 27 Aug. 2004.  
\*Corresponding author (michael.nicholl@ccmail.nevada.edu).

Published in Vadose Zone Journal 4:1123–1151 (2005).

Original Research

doi:10.2136/vzj2004.0110

© Soil Science Society of America

677 S. Segoe Rd., Madison, WI 53711 USA



**Fig. 1.** Cliff face showing an approximately 10-m high exposure of fractured basalt located in southeastern Idaho (Schaefer, 2002). Extensive vertical fractures formed during cooling of the molten lava dominate the fracture network, which also includes a smaller number of less extensive subhorizontal fractures. The horizontal recess is a sedimentary interbed.

Next (Experimental Observations: Single Fingers from Point Sources), we consider individual fingers initiated from steady flow to a point source. Measured data are presented in Quantitative Evaluation of Finger Behavior, followed by the development of simple predictive relations for finger width and fingertip length as functions of finger velocity, with comparison with measured data. In Experimental Observations: Illustrative Extensions to our Principal Results, we present a series of illustrative experiments intended to guide future work. We consider (i) a modification to our principal analog fracture that alters the balance between forces, (ii) micro-roughness on the fracture surfaces, (iii) natural fracture aperture fields, (iv) imbibition by the adjacent matrix, and (v) buoyant nonwetting fingers. We then conclude with a summary of our key observations, followed by an introduction to the related areas of network-scale flows and non-wetting displacement by dense nonaqueous phase liquids (DNAPLs).

## BACKGROUND AND THEORETICAL FRAMEWORK

This section outlines results from related areas that guided our investigation. We begin with the general topic of immiscible displacement in fractures. Then we review linear stability analysis of rectilinear displacement in the Hele-Shaw geometry and customize relations developed in that context to the infiltration of water into an air-filled system.

## Fractures and Immiscible Displacement

Fracture flow occurs within the void space, or aperture between two uneven surfaces that result from brittle failure. This variable-aperture field determines the permeability of the fracture. Aperture variability also places important controls on the immiscible displacement of one fluid by another, and progress has been made with respect to capillary dominated (i.e., slow and horizontal) displacements.

## Fracture Aperture Fields

Fracture surfaces can span from very rough (such as tectonic fractures in plutonic granites) to relatively smooth (such as columnar cooling fractures in volcanic rocks as seen in Fig. 1). A number of measurements on rough fracture surfaces have suggested a self-affine fractal topography at length scales from the submillimeter upward (e.g., Brown and Scholz, 1985; Poon et al., 1992; Schmittbuhl et al., 1995). However, the smoother surfaces of cooling fractures in volcanic rock or fractures in glasses tend to lack a fractal quality at the smaller scales (e.g., Throckmorton and Verbeek, 1995). Plastic deformation and disaggregation following brittle failure will usually prevent the surfaces from mating perfectly, as will small displacements between the two surfaces (e.g., Plouraboue et al., 1995). A gap or aperture field is thus created that varies from point to point and may include contact areas where the aperture,  $a$  (L), goes to zero. Initial fracture topology may be subsequently



modified by additional movement, the dissolution and precipitation of minerals, and/or mechanical erosion of the fracture surfaces (e.g., National Research Council, 1996; Hanna and Rajaram, 1998; Weisbrod et al., 1998, 2000; Streit and Cox, 2000; Durham et al., 2001).

Although the topology of natural fractures exhibits extreme variability, there are expected commonalities that can be used to constrain fracture aperture fields for the study of gravity-driven fingering in the laboratory. Displacement of one fracture surface with respect to the other will disrupt long-range correlations between the surfaces and impose a maximum length scale on spatial correlation in the aperture field (e.g., Brown, 1995; Plouraboue et al., 1995). Detailed aperture characterizations are scarce; however, the aperture spatial correlation length,  $\lambda$ , has been estimated in the laboratory through X-ray tomography (Keller, 1998) of naturally fractured granite cores ( $\lambda \approx 0.08$ – $1.2$  cm), destructive sectioning (Hakami and Larsson, 1996) of an epoxy filled natural granite fracture ( $\lambda \approx 1$  cm), and light absorption within cast replicas (Lee et al., 2003) of artificially fractured sandstone ( $\lambda \approx 0.6$ – $3.8$  cm). Additionally, below a certain length scale, fracture surfaces, and thus aperture, will become smooth. This lower limit will not only vary with the rock material, but also be greatly influenced by precipitation and dissolution processes. Finally, because most fractures require some propping to remain open (such as occurs in translation along the rough surface), many fractures have mean apertures in the range where capillary forces are important (i.e., below  $0.1$  cm). The investigations referenced above estimated mean aperture,  $\langle a \rangle$ , at  $0.0639$  to  $0.0825$  cm (Keller, 1998),  $0.36$  cm (Hakami and Larsson, 1996), and  $0.0259$  to  $0.0384$  cm (Lee et al., 2003).

### Fracture Permeability

Steady flow through a fracture at low Reynolds number ( $Re < 10$ ) is commonly assumed to follow Darcy's Law. For a fracture filled with a single fluid phase, flux,  $q$  ( $L T^{-1}$ ), will be linearly dependent on the hydraulic gradient, with the constant of proportionality given by the saturated hydraulic conductivity,  $K_s$  ( $L T^{-1}$ ):

$$K_s = \frac{k\rho g}{\mu} \quad [1]$$

where  $k$  represents intrinsic permeability of the fracture ( $L^2$ ),  $\rho$  is fluid density ( $M L^{-3}$ ),  $g$  is the gravitational constant ( $L T^{-2}$ ), and  $\mu$  is the fluid kinematic viscosity ( $M/LT$ ). Attempts to parameterize  $k$  for rough-walled fractures have confirmed that aperture variability leads to a deviation from the Hele-Shaw result where  $k = a^2/12$  (e.g., Brown, 1989; Zimmerman and Bodvarsson, 1996; Nicholl et al., 1999).

The presence of two or more fluids within a fracture leads to phase interference, and permeability to each will be less than  $k$  (e.g., Fourar et al., 1993; Murphy and Thomson, 1993; Persoff and Pruess, 1995; Nicholl et al., 2000). The reduction in permeability is often represented by the relative permeability,  $k_r$ , a dimensionless fraction that varies between  $0$  and  $1$ . Under most natural

hydrologic conditions, water either displaces the air phase as it invades a fracture, or air reinvades as water drains. In both cases, incomplete displacement and an absence of film flow may lead to a phase structure in which only one phase is free to flow, while the other occupies entrapped zones that obstruct flow. Because the connectivity of fracture void space is essentially two-dimensional, entrapped zones have a much larger influence on permeability than in three-dimensional porous media.

### Capillary Displacement in Fractures

Capillary forces impose a pressure jump,  $P_c$  ( $F L^{-2}$ ), across the interface between two immiscible fluids (e.g., air and water). In the absence of viscous and gravity forces (e.g., slow horizontal flow),  $P_c$  along the interface provides the sole control on displacement, and thus fluid phase structure. Under these quasistatic conditions,  $P_c$  is dependent on the local interfacial curvature as given by the Laplace–Young equation:

$$P_c = \sigma(r_1^{-1} + r_2^{-1}) \quad [2]$$

where  $\sigma$  is the interfacial tension ( $M T^{-2}$ ),  $r_1$  is the first principal radius of interfacial curvature ( $L$ ), and  $r_2$  is the second principal radius of curvature ( $L$ ). For a variable-aperture fracture,  $r_1$  spans the two walls of the fracture, while  $r_2$  lies in the plane of the fracture (Fig. 2). Thus,  $r_1$  is constrained by the fluid–fluid–solid contact angle,  $\alpha$ , while  $r_2$  is not (National Research Council, 1996). Where fracture aperture varies symmetrically about a mean plane (Fig. 2b),  $r_1$  can be written as

$$r_1 = \frac{a}{2\cos(\alpha + \beta)} \quad [3]$$

where  $\beta$  describes the local change in aperture. The second principal radius of curvature evolves as the interface grows (Fig. 2a). Within a spatially correlated random field,  $r_2$  can be approximated as (Glass et al., 1998)

$$r_2 = (\lambda/2) \tan(\phi/2) \quad [4]$$

where  $\phi$  is the angle between two vectors that approximate the local interface, as measured from the displacing fluid side (Fig. 2b).

Modified Invasion Percolation (MIP) simulations that embody Eq. [2] to [4] have shown that phase structure during capillary displacement in a variable-aperture field is controlled by the competition between interfacial roughening due to random aperture ( $r_1$ ) variations and interfacial smoothing due to in-plane ( $r_2$ ) curvature (Glass et al., 1998). To first order, phase structure is determined by the Curvature number,  $C$ , a dimensionless parameter formed as a ratio of representative values for each influence:

$$C = \frac{\langle a \rangle}{\lambda \cos \alpha} \quad [5]$$

Later, Glass et al. (2003) found that the ratio  $C/\delta$  more comprehensively controls phase structure, where  $\delta$  represents the coefficient of variation ( $L L^{-1}$ ) for the aperture field. For  $C/\delta$  well below  $1$ , aperture-induced curvature dominates, and the phase structure is controlled

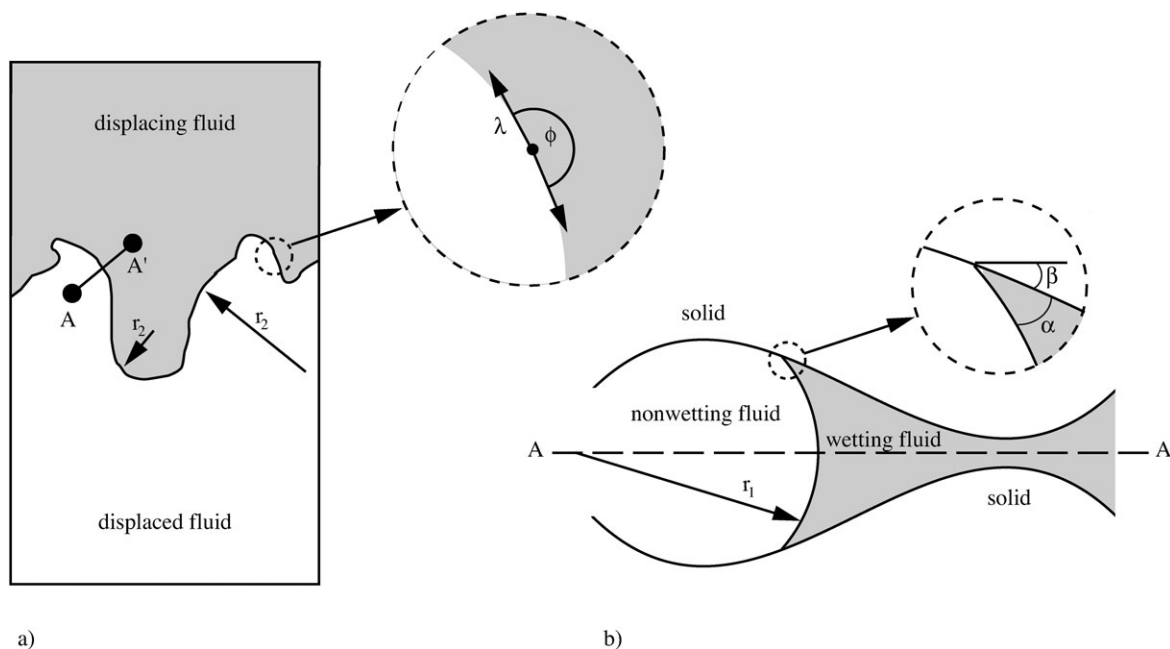


Fig. 2. (a) Sketch illustrating the fluid–fluid interface in plan view (not to scale). In-plane curvature,  $r_2$ , is shown at two different locations, while the inset depicts the approximation of  $r_2$  in Eq. [4]. (b) Cross-sectional view along the line A–A' (Fig. 2a) depicts the definition of  $r_1$ . Inset shows  $\alpha$  and  $\beta$  from Eq. [3].

by capillary fingering within the spatially correlated field. As  $C/\delta$  increases, capillary fingers widen to above the spatial correlation length. For  $C/\delta$  well above 1, the interface is dominated by  $r_2$  curvature, and thus behaves as though in a Hele-Shaw cell, with little or no entrapment of the defending phase.

Finally, we note that, just as in porous media, capillary invasion pressures for fractures are different for wetting and nonwetting fluids. A number of processes lead to hysteresis. The most important is that nonwetting invasion is controlled by the large apertures within the field, while wetting invasion is controlled by the smaller ones. Second-order influences come from contact angle hysteresis and dynamics, where the wetting angle is often larger than the drainage angle (e.g., Dussan, 1979; de Gennes, 1985). The combination of these influences changes the distribution of apertures that are sampled between nonwetting and wetting invasion and, through interaction with  $r_2$ , yields differences in the displacement phase structures. In essence, wetting phase invasion has a higher  $C/\delta$  and a correspondingly more macroscopic phase structure than nonwetting invasion (Glass et al., 2003).

### Results from Linear Stability Theory in a Hele-Shaw Cell

Linear theory has been used to consider the stability of rectilinear displacement in a Hele-Shaw cell (e.g., Saffman and Taylor, 1958; Chouke et al., 1959; Saffman, 1986; Homsy, 1987), which is essentially a constant aperture fracture. In the absence of capillarity, rectilinear displacement of one incompressible viscous fluid (subscript 1) by another (subscript 2) along the plane of a Hele-Shaw cell is expected to be unstable to perturba-

tions of all wavelengths when the following inequality is satisfied (after Chouke et al., 1959):

$$\frac{U}{k}(\mu_2 - \mu_1) < (\rho_2 - \rho_1)g\cos\theta \quad [6]$$

where  $U$  is interfacial velocity ( $L T^{-1}$ ) in the direction of displacement and  $\theta$  is the included angle between the direction of displacement and the vertical downward direction (i.e.,  $\cos\theta$  is positive for downward displacement). This simple linear analysis suggests that gravity-driven fingers will form where a destabilizing gravitational force (i.e., right-hand side of Eq. [6] is positive) is not offset by a stabilizing viscous force of equal or greater magnitude.

Assuming displacement in a Hele-Shaw cell where the fluid–fluid interface is perturbed at all wavelengths, the linear analysis used to develop Eq. [6] predicts that the shortest wavelength perturbations will experience the most rapid growth (e.g., Homsy, 1987). However, for immiscible fluids, surface tension will act to preferentially damp short wavelengths. Competition between these two wavelength-dependent influences (growth rate and dampening) will act to select a single wavelength for maximum growth rate,  $\lambda_m$  (Chouke et al., 1959):

$$\lambda_m = 2\pi\sqrt{3\sigma}\left[(\rho_2 - \rho_1)g\cos\theta - \frac{U}{k}(\mu_2 - \mu_1)\right]^{-1/2} \quad [7]$$

Noting that fingers are expected to form at widths on the order of  $\lambda_m/2$ , Eq. [7] suggests that finger width will be determined by both interfacial tension and the degree of instability as expressed by the bracketed term.

### Unstable Infiltration

Specialization of Eq. [6] to infiltration is straightforward. Water closely approximates an incompressible

viscous fluid, while air may be treated as an inviscid fluid of negligible density that escapes freely during displacement. Under these conditions, Eq. [6] may be restated as

$$U < K_s \cos \theta \quad [8]$$

which suggests that gravity-driven fingers are likely to form at infiltration velocities  $< K_s \cos \theta$ . Because  $K_s \cos \theta$  gives the flux for saturated flow influenced by gravity alone, we see that local capillary forces, heterogeneity within the field, or external pressure can act to stabilize or destabilize infiltration. Simplification of Eq. [7] to displacement of air by water leads to

$$\lambda_m = 2\pi\sqrt{3} \left( \frac{\sigma}{\rho g \cos \theta} \right)^{1/2} \left( 1 - \frac{U}{K_s \cos \theta} \right)^{-1/2} \quad [9]$$

We note, however, that the simple action of capillarity put forth in Eq. [7] is only strictly valid within a Hele-Shaw cell. There, the aperture induced component of the capillary force,  $r_1$  in Eq. [2], is of equal value everywhere along the interface, thus leaving the in-plane component,  $r_2$  in Eq. [2], to smooth or stabilize the front. In a variable-aperture field,  $r_1$  related capillary forces will vary along the fluid-fluid interface, yielding some deviation from relations such as Eq. [7] and [9] that assume constant  $r_1$ . Analogous discrepancies are also relevant for porous media (e.g., Chouke et al., 1959; Parlange and Hill, 1976).

Experiments in granular porous media provide additional information that is germane to our study of gravity-driven fingering in fractures. Infiltration into narrowly distributed dry sands has been found to be unstable for (i) steady supply (e.g., rainfall) at  $q < K_s \cos \theta$  (e.g., Selker et al., 1992a), (ii) steady supply where  $K_s$  increases with depth (e.g., Hill and Parlange, 1972; Diment and Watson, 1985; Glass et al., 1989b), and (iii) redistribution following viscous controlled infiltration (e.g., Raats, 1973; Philip, 1975; Jury et al., 2003; Wang et al., 2003a, 2003b). It has also been found that individual fingers in initially dry sands consist of a saturated tip, followed by a partially desaturated zone (Glass et al., 1989c; Selker et al., 1992b). Glass et al. (1989c) related length of the saturated fingertip,  $L_{tip}$ , to fingertip velocity,  $v$  ( $L T^{-1}$ ), through Darcy's Law:

$$v = K_s \left[ 1 - \frac{\psi_w - \psi_d}{L_{tip}} \right] \quad [10]$$

where  $\psi_w$  is the wetting pressure head (L) for the media, and  $\psi_d$  is the drainage pressure head (L). Due to capillary hysteresis,  $\psi_d$  will be more negative than  $\psi_w$  in water-wettable porous media; thus, the bracketed term in Eq. [10] will not exceed one, and  $v \rightarrow 0$  when  $L_{tip} = \psi_w - \psi_d$  (see also Wang et al., 2004).

Hysteresis also causes finger locations to persist from one infiltration cycle to the next (e.g., Glass et al., 1988, 1989a; Liu et al., 1994). Conversely, uniform moisture fields have been found to widen, or even suppress the formation of gravity-driven fingers (Diment and Watson, 1985; Glass and Nicholl, 1996; Wang et al., 2003a, 2003b). While the exact value of moisture content re-

quired to suppress instability remains open, it is likely to be defined by the point at which liquid films can be maintained on the surface of grains (Glass and Nicholl, 1996).

## EXPERIMENTAL DESIGN

Exploration of gravity-driven fingering in fractures requires that we be able to control and/or vary the influence of capillary, gravity, and viscous forces in a systematic fashion. It must also be possible to measure and observe behavior without perturbing the flow field. To meet these objectives, we used textured glass plates to fabricate analog fractures that were transparent, water wettable, and reproducible. Between experiments we held the fracture geometry constant, and altered the balance between capillary and gravity forces by varying the angle of the fracture within the gravitational field. We considered two different boundary conditions at the top of the fracture: (i) ponding followed by redistribution and (ii) constant supply to point sources where single fingers initiate from the controlled perturbation. In both cases, we varied viscous forces between experiments by altering the fluid application (pond volume for redistribution, supply rate for single fingers). Given the strong influence of antecedent moisture observed in porous media, we also varied initial conditions within the analog fracture from dry to partially saturated, with particular emphasis on structure of the initial moisture field. In this section, we present details of the experimental system, the measured properties of the analog fracture, and outline the experiments performed.

### Experimental System

Aperture fields were fabricated in two sizes, 30 by 60 cm and 15 by 30 cm; the larger size was used to consider systems characterized by multiple fingers, while the smaller one was used to focus in on the behavior of individual fingers. For both sizes, displacement was directed in the long axis. Confinement cells constructed to hold the experiment (Fig. 3a) were pressurized with gas to place the analog fractures under a 0.138 MPa (20 psi) normal load. The normal pressure held the textured glass plates in close contact, eliminating long wavelength disturbances in the aperture fields. Windows in each cell allowed us to view almost the entire aperture field (except for a border of  $\approx 1$  cm along the edges). The cell design also allowed us to implement various boundary conditions and to reassemble the aperture fields in a repeatable alignment. In preliminary trials to test reproducibility, we found it necessary to carefully clean and dry the glass surfaces between experiments. It was also important to follow a strict protocol while first assembling the cell, and then torquing the bolts that hold it together (Fig. 3a). In the course of our experiments the textured plates broke several times and were replaced.

Data were obtained from sequential images collected during each experiment. The confinement cells were clamped onto a light table that includes a steel superstructure designed to hold a CCD camera ( $512 \times 512$  pixel, 8-bit resolution) at a fixed location above the

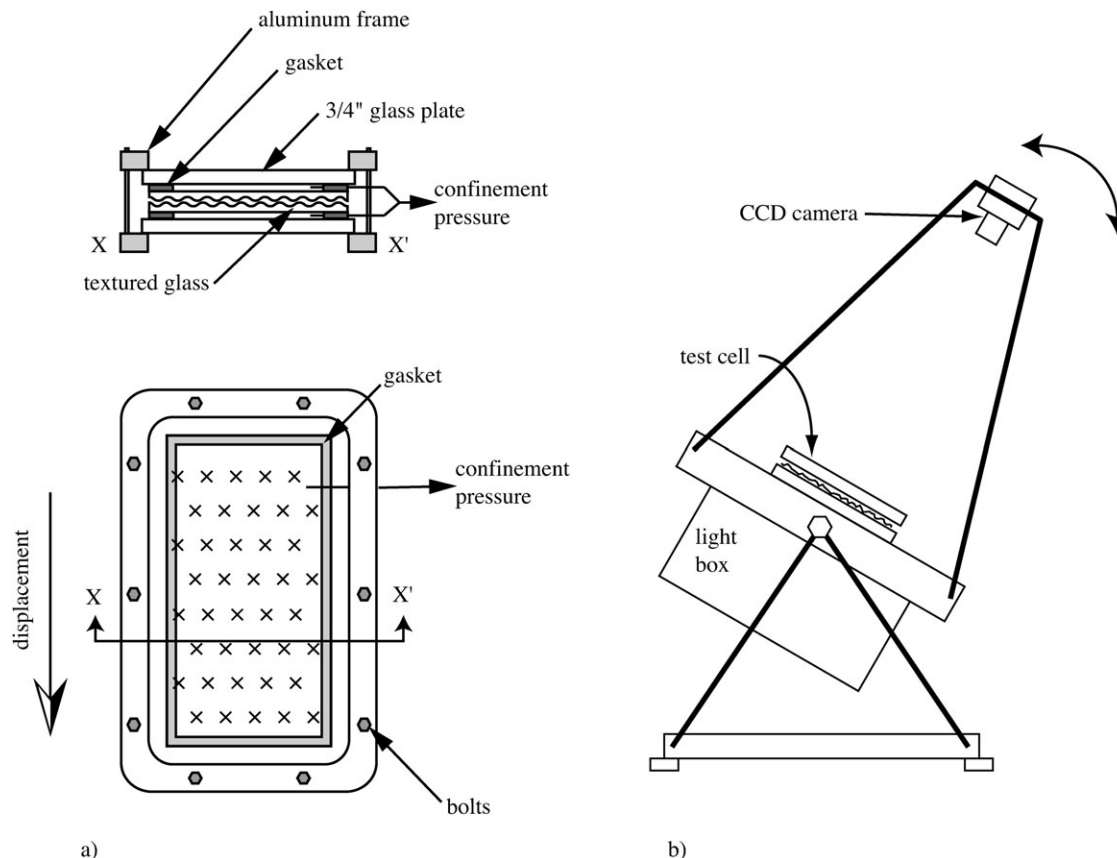


Fig. 3. a) Sketches of our 15- by 30- and 30- by 60-cm test cells in plan and cross-sectional views (not to scale). Each of the textured glass plates is separated from a 19-mm (3/4") glass plate window by a thin rectangular gasket. A needle inserted through the gasket allows pressurization of the intervening space, pushing the two textured plates into close contact. Note that a larger number of bolts than shown were used to assemble the 30- by 60-cm cell. (b) Sketch of our test stand (not to scale). Light intensity is controlled through a feedback circuit. The light box also contains a cooling system to prevent warming the experiment.

experiment (Fig. 3b). The whole apparatus (light table, confinement cell, and CCD camera) could be rotated as a unit to allow variation of the gravity force through fracture inclination (i.e.,  $\cos\theta$ ). The amount of light transmitted through the analog fracture was modified locally by the presence of air, deionized water, or dyed water. Dyes (FD&C Blue #1 and Red #3) were added to deionized water in concentrations of  $1 \text{ g L}^{-1}$  or less; simple tests assured that addition of the dye imposed a negligible influence on fluid properties.

### Analog Fracture Properties

The textured glass plates used in our experiments were selected from a category of decorative materials known as obscure glass. We examined various textures and selected one that would produce homogenous, isotropic aperture fields within the range of natural fractures, and exhibit  $C/\delta$  between the extremes of  $r_1$  or  $r_2$  domination. The analog fractures were water-wettable, with a static contact angle of 35 to 55°. The pattern of the textured glass plates used in our experiments can be clearly seen in the aperture field produced when one textured plate is pressed up against a smooth glass plate (Fig. 4a) as measured by transmitted light imaging (e.g., Detwiler et al., 1999). For our experiments, two textured plates were assembled in face-to-face contact to produce

an aperture field as seen in Fig. 4b. In both instances, the 3- by 3-cm segments shown in the figure are representative of the entire aperture field. Aperture distributions for both fields are shown in Fig. 4c. Aperture statistics are provided in Table 1, along with hydraulic and capillary measurements. Vertical capillary rise was measured as an estimate of the wetting pressure head ( $\psi_w$ ), while the drainage pressure head ( $\psi_d$ ) was taken as the fluid height after free drainage. By design, the characteristic length scale of the aperture variability (Fig. 4d) is much smaller ( $\lambda \approx 0.08 \text{ cm}$ ) than the experiments (15 by 30 and 30 by 60 cm). The resulting analog fractures are homogenous and isotropic at the macroscopic scale, thus assuring that observed behavior is controlled by the processes under study rather than heterogeneity-driven channeling. Finally, we note that the statistical measures of our analog fractures ( $\langle a \rangle$ ,  $\delta$ ,  $\lambda$ ) fall within the range of those reported for natural fractures (e.g., Johns et al., 1993; Hakami and Larsson, 1996; Keller, 1998; Su et al., 1999).

### Experiments Conducted

Our experimental investigation of gravity-driven fingering in fractures included a large number of experiments conducted during approximately 10 yr. A small portion of these experiments were published in Nicholl



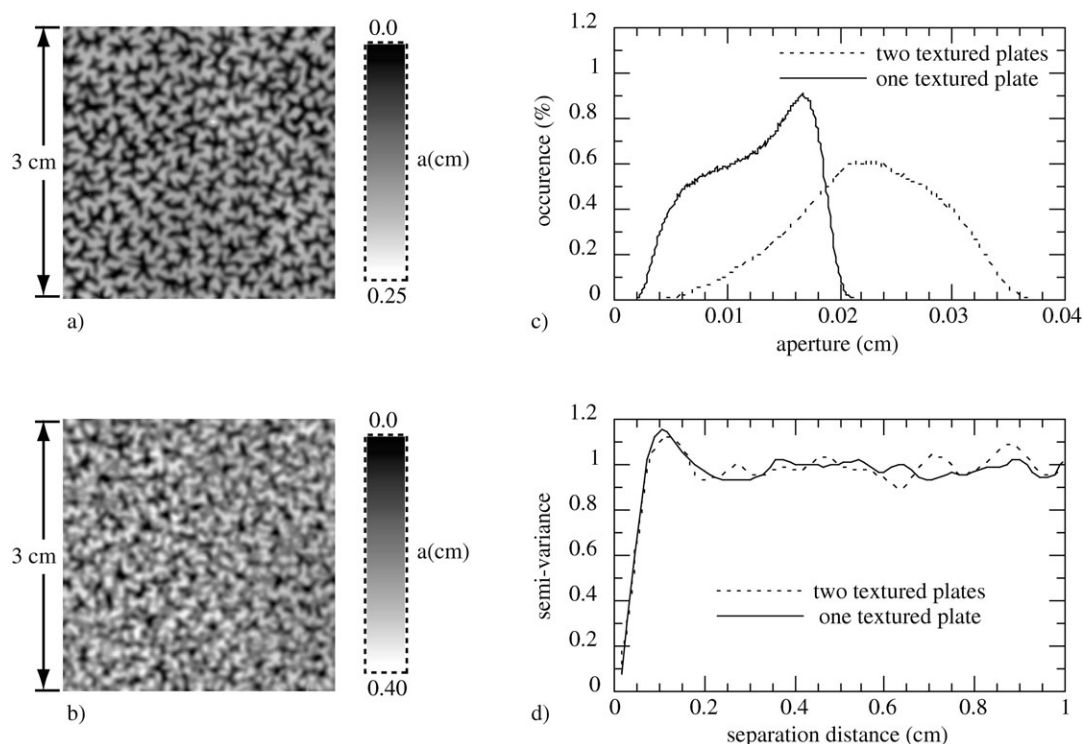


Fig. 4. (a) A 3- by 3-cm segment representative of the aperture field formed when one of our textured glass plates is held against a smooth glass plate. Dark regions (small aperture) correspond to raised bumps on the surface of the textured plates. (b) 3- by 3-cm segment representative of the aperture field formed when two of our textured glass plates are held in face-to-face contact. (c) Aperture distributions. (d) Spatial correlation within the aperture field. Note the negative correlation, or hole, in the variogram at separation distances of approximately 0.08 to 0.17 cm ( $\approx 1-2\lambda$ ). Measurements were made by Nicholl et al. (1999), using transmitted light imaging techniques developed by Detwiler et al. (1999).

et al. (1994); additional preliminary results were presented at conferences (Nicholl et al., 1992, 1993a, 1993b), and mentioned in Glass and Nicholl (1996). Given the extent of our experimental investigations, we have chosen to present a synthesis of results that highlights the major observations across experiments. Experimental Observations: Multiple Fingers as Generated via Redistribution Following Ponding Events considers gravity-driven fingers formed following ponded infiltration of water into fractures both with and without antecedent moisture content. Experimental Observations: Single Fingers from Point Sources focuses on gravity-driven fingers generated from single point sources, again with and without antecedent moisture content. In Quantitative Evaluation of Finger Behavior, measured data are evaluated, and a simple local force balance is employed to develop relationships for fingertip length and finger width as functions of finger velocity. Finally in Experimental Observations: Illustrative Extensions to our Principal Results, we extend our principal results with a set of illustrative experiments designed to guide future work.

## EXPERIMENTAL OBSERVATIONS: MULTIPLE FINGERS AS GENERATED VIA REDISTRIBUTION FOLLOWING PONDING EVENTS

One of the most ubiquitous situations that can lead to gravity-driven fingers is the redistribution of flow that follows a rainfall or irrigation event (e.g., Raats, 1973; Philip, 1975; Jury et al., 2003; Wang et al., 2003a, 2003b). We simulated such a situation by rapidly ponding a finite volume of water in a shallow reservoir that covered the top edge of our 30- by 60-cm analog fracture. All other edges of the fracture were left open to atmospheric pressure so air could freely escape. Over a series of experiments, the volume of water added to the pond was varied to explore the influence of viscous forces. Fracture inclination (i.e.,  $\cos\theta$ ) was varied to consider gravity forces. First, we consider infiltration into a dry fracture, then look at the influence of initial moisture.

### Initially Dry Fractures

We conducted 24 experiments to consider ponded infiltration into an initially dry fracture. Four values of

Table 1. Aperture statistics and hydraulic and capillary measurements.

Textured plates used	$\langle a \rangle^\dagger$	$\delta^\dagger$	$\lambda^\dagger$	$C$	$C/6$	$K_s^{\dagger\ddagger}$	$\psi_w$	$\psi_d$
	cm		cm			$\text{cm s}^{-1}$		cm
Smooth-textured	0.01240	0.3572	0.08	0.155	0.434	0.83	-3.65	-7.43
Two-textured	0.02255	0.2742	0.08	0.282	1.03	3.2	-2.25	-5.10

$^\dagger$  Nicholl et al. (1999).

$^\ddagger$  At 25°C.

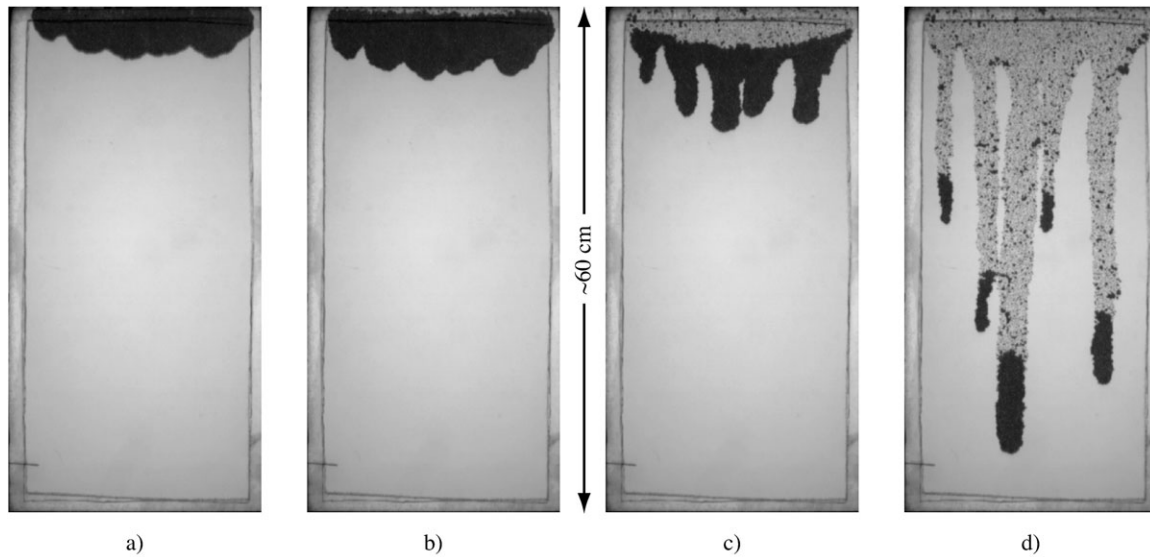


Fig. 5. The formation of gravity-driven fingers following ponded infiltration ( $V_p = 4.29 \text{ cm}^3$ ) into the initially dry 30- by 60-cm cell at  $\cos\theta = 1.0$ .

$\cos\theta$  were considered (1.0, 0.75, 0.50, and 0.25). Input volume to the pond,  $V_p$  ( $\text{L}^3$ ), was varied over a range from 3.4 to 28.4  $\text{cm}^3$ ; note that total aperture volume of the analog fracture was about 41  $\text{cm}^3$ . The analog fracture was disassembled, cleaned, and dried between trials.

Digital images of fluid advancement (Fig. 5) show the transition from initially stable to unstable infiltration where gravity-driven fingers form. Water is added to the pond from 16 evenly spaced point sources. This slight nonuniformity introduces finite-amplitude perturbations to the fluid–fluid interface. With water in the pond (Fig. 5a) capillary forces act only along the leading edge of the fluid slug, where they reinforce gravity. As a result, interfacial velocity is high ( $U > K_s \cos\theta$ ) and viscous forces preferentially focus flow into the least advanced portions of the leading edge, damping initial perturbations (i.e., flow is stable). When fluid in the pond is exhausted, gravity acting on the fluid slug exerts tension along the trailing edge of the slug and initiates drainage (Fig. 5b). Drainage pressures along the trailing edge of the fluid slug act to oppose gravity and are of greater magnitude than the wetting pressures that reinforce gravity along the leading edge. Thus, capillary forces within the fluid slug reverse direction and oppose flow. Interfacial velocity decreases ( $U < K_s \cos\theta$ ), and flow is preferentially redistributed into the furthest advanced portions of the front (perturbations grow) (i.e., flow is unstable).

At the onset of instability, gravity-driven fingers begin to develop from the most dominant perturbations to the front and take on the characteristic width of those perturbations (Fig. 5c). While the fluid slug is intact (i.e., laterally connected) individual fingers compete for fluid, such that larger and more advanced fingers grow at the expense of their smaller neighbors. Fingers eventually separate from one another to fragment the slug and become distinct entities (Fig. 5d) that move as compact bodies, leaving behind a trail of small fluid blobs pinned within the aperture field. Fingertip length de-

creases in response to fluid loss during advancement. Because the capillary force that resists movement is inversely proportional to fingertip length, fingers slow as they lose fluid, and eventually stop when gravitational forces are balanced by capillary forces. The smallest two fingers seen in Fig. 5d stalled within the fracture. If the fracture had been longer, the other three fingers would eventually have stopped.

Although much smaller than their parent fingers, the fluid blobs left behind following passage of the fingertip (Fig. 5b–5d) are often considerably larger than the spatial correlation length of the aperture field,  $\lambda$ . This observation suggests that water is retained in apertures of all sizes. The drainage process involves a reinvasion along the trailing edge of the saturated fingertip by the nonwetting air phase. The reinvasion process entraps water and pins it within the aperture field in accordance with the local balance between capillary, viscous, and gravitational forces. When compared with the smooth fingertip, the differences between wetting and nonwetting invasion at similar  $C/\delta$  (Glass et al., 1998, 2003) produces a much more complicated interface along the trailing edge.

Across all experiments, the finite amplitude perturbations present at the time of redistribution control the width of subsequent fingers. In our experiments, viscous damping of the initial perturbations increased with distance traveled before redistribution. In Fig. 5b, the 16 perturbations induced by fluid application damped into five in the short distance between the top edge of the fracture and the onset of redistribution. As illustrated in Fig. 6, larger pond volumes increase the viscous damping before redistribution, which acts to increase finger width and reduce the number of fingers. Variation of fracture inclination showed little if any effect on finger width. However, increasing  $\cos\theta$  did lead to faster and somewhat smoother fingers that more closely follow the gravitational vector (Fig. 7).

In order for redistribution to proceed after the pond is depleted the fluid slug must exert sufficient tension



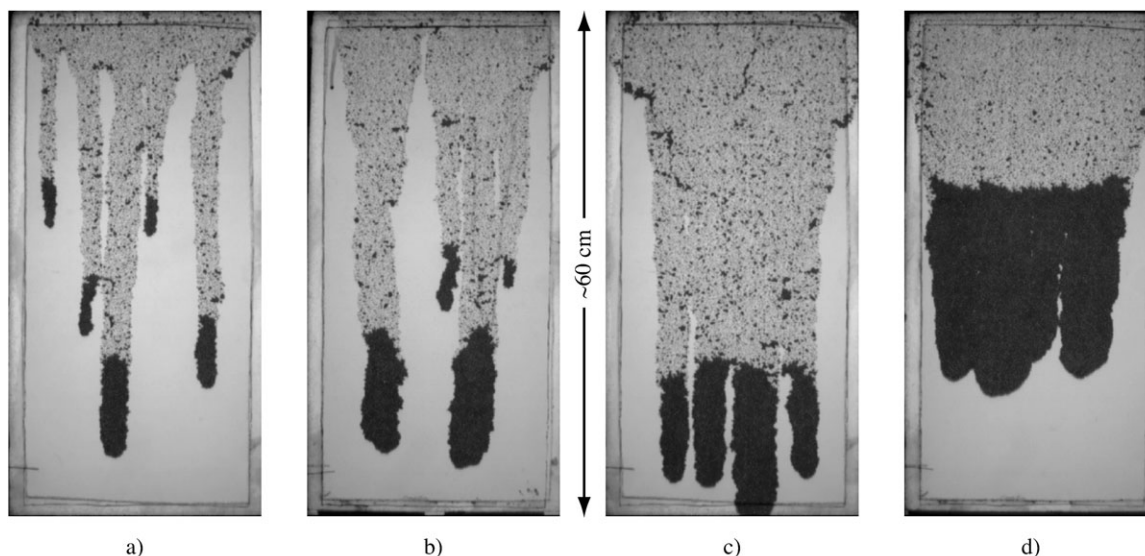


Fig. 6. The effects of pond volume,  $V_p$ , on fingers formed in the initially dry 30- by 60-cm cell at  $\cos\theta = 1.0$ . Image time in seconds after starting the experiment ( $t$ ) gives an indication of relative velocity. (a)  $V_p = 4.29 \text{ cm}^3$ ,  $t = 23 \text{ s}$ ; (b)  $V_p = 6.17 \text{ cm}^3$ ,  $t = 23 \text{ s}$ ; (c)  $V_p = 10.23 \text{ cm}^3$ ,  $t = 23 \text{ s}$ ; and (d)  $V_p = 14.06 \text{ cm}^3$ ,  $t = 15 \text{ s}$ .

to initiate drainage. Otherwise it will remain pinned within the fracture. Note that tension applied by the slug is given by the vertical distance between the leading and trailing edges of the slug. The fluid slug shown in Fig. 8 appears to be pinned in place after the pond is depleted (Fig. 8a). However, for the next  $\approx 10$  min drainage along the top of the fracture proceeds on a very slow ("pore-by-pore") basis. Tension applied by the fluid slug is about 1.4 cm, much less than the average drainage pressure of  $-5.1 \text{ cm}$  (Table 1). As a result, drainage is restricted to the largest apertures (see top edge of Fig. 8b), with the drained fluid being redistributed to the tip of the most advanced perturbation (see circled region in Fig. 8b). The perturbation grows slowly for about the next 10 min (Fig. 8c), then accelerates and widens substantially during the next 5 min (Fig. 8d). At this

point, tension exerted by the finger ( $\approx 4.9 \text{ cm}$ ) is of similar order to the drainage pressure, and thus drainage involves a wider range of apertures. Locally, tension generated within the growing finger is sufficient to initiate drainage within the narrow neck connecting it to the original fluid body (see circled region in Fig. 8d).

### Influence of Initial Moisture

As discussed above, experimental studies in hydrophilic sands suggest that gravity-driven fingers formed under initially dry conditions will persist to create preferential pathways for subsequent infiltration events. To explore this possibility, we conducted 31 experiments where the fracture contained a structured initial moisture field created by a previous unstable infiltration

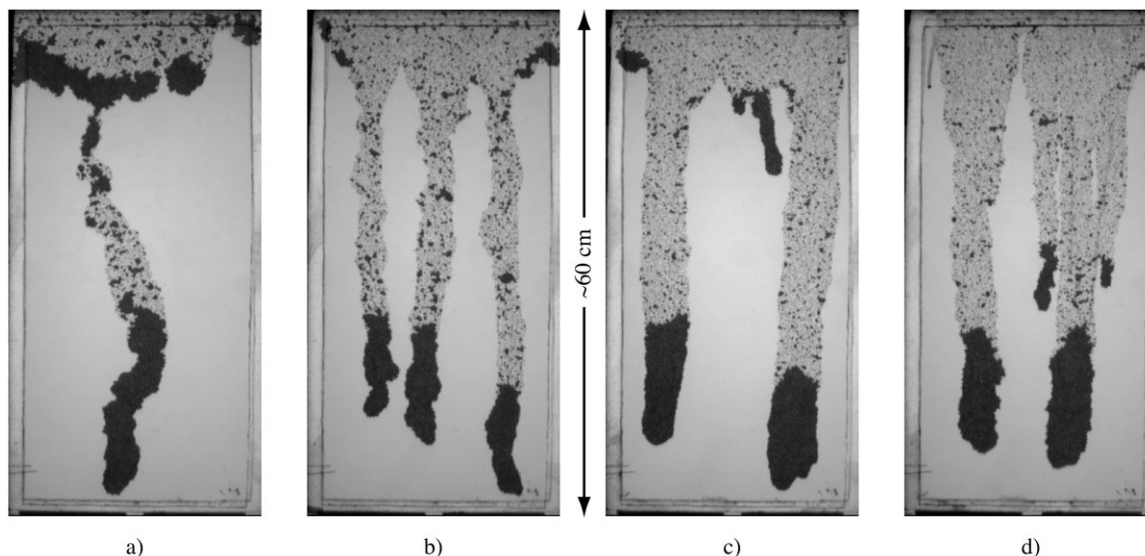
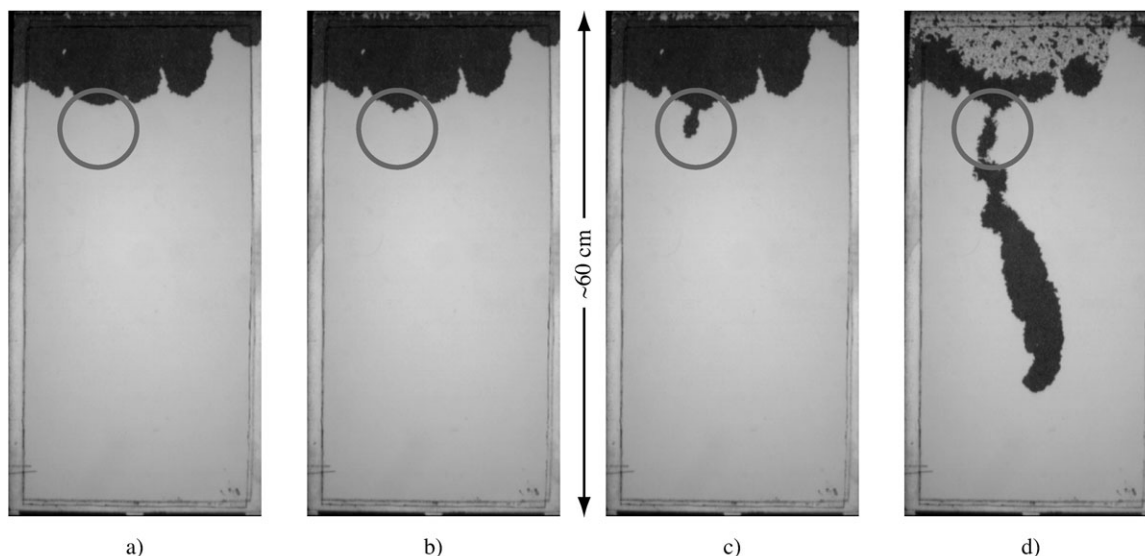


Fig. 7. The effects of  $\cos\theta$  on fingers formed following ponded infiltration into the initially dry 30- by 60-cm cell at similar  $V_p$ . Image times give an indication of relative velocity. (a)  $\cos\theta = 0.25$ ,  $V_p = 6.23 \text{ cm}^3$ ,  $t = 1593 \text{ s}$ ; (b)  $\cos\theta = 0.50$ ,  $V_p = 6.10 \text{ cm}^3$ ,  $t = 63 \text{ s}$ ; (c)  $\cos\theta = 0.75$ ,  $V_p = 6.47 \text{ cm}^3$ ,  $t = 39 \text{ s}$ ; and (d)  $\cos\theta = 1.0$ ,  $V_p = 6.17 \text{ cm}^3$ ,  $t = 23 \text{ s}$ .



**Fig. 8.** Slow growth of a single finger following ponded infiltration ( $V_p = 6.23 \text{ cm}^3$ ) into the initially dry 30- by 60-cm cell at  $\cos\theta = 0.25$ . Image times give an indication of relative velocity. (a)  $t = 39 \text{ s}$ ; (b)  $t = 619 \text{ s}$ ; (c)  $t = 1211 \text{ s}$ ; and (d)  $t = 1518 \text{ s}$ .

event. Experiments were conducted at  $\cos\theta = 1.0, 0.75$ , and  $0.50$ ;  $V_p$  was varied over a range from  $3.75$  to  $26 \text{ cm}^3$ . We also conducted five experiments in which the fracture contained a uniformly distributed initial moisture field.

The structured initial moisture field created by unstable infiltration was found to guide subsequent events. Figure 9a shows the moisture structure present at the conclusion of the experiment shown in Fig. 5; three fingers have passed through to the bottom of the cell, while two have stalled and are pinned within. A second ponding event of similar magnitude ( $V_p = 4.2 \text{ cm}^3$ ) to the first ( $4.3 \text{ cm}^3$ ) follows the initial moisture structure (Fig. 9b and 9c). The second event entraps significant amounts of air to form fingers that are not only much longer than were observed under dry initial conditions, but also exhibit a complex internal structure that was not present in the dry fracture (Fig. 5d). The second

event loses little, if any, fluid as it passes through the initial moisture structure to restart the stalled fingertips (Fig. 9d). Fluid loss begins when the second event exits the initial moisture structure and continues to advance, as was observed under dry initial conditions.

In experiments where the second ponding event was of substantially smaller magnitude than the initial event, we observed fingers that were much narrower than those that created the initial moisture field. This observation conflicts with experimental results for granular porous media, where it has been found that a uniform initial moisture field provides a stabilizing influence that widens or suppresses gravity-driven fingers (Diment and Watson, 1985; Glass and Nicholl, 1996; Wang et al., 2003a, 2003b). To explore this apparent conflict, we conducted five additional redistribution experiments for “uniform” initial moisture fields. We saturated the 30- by 60-cm cell, then rotated it to the desired inclination

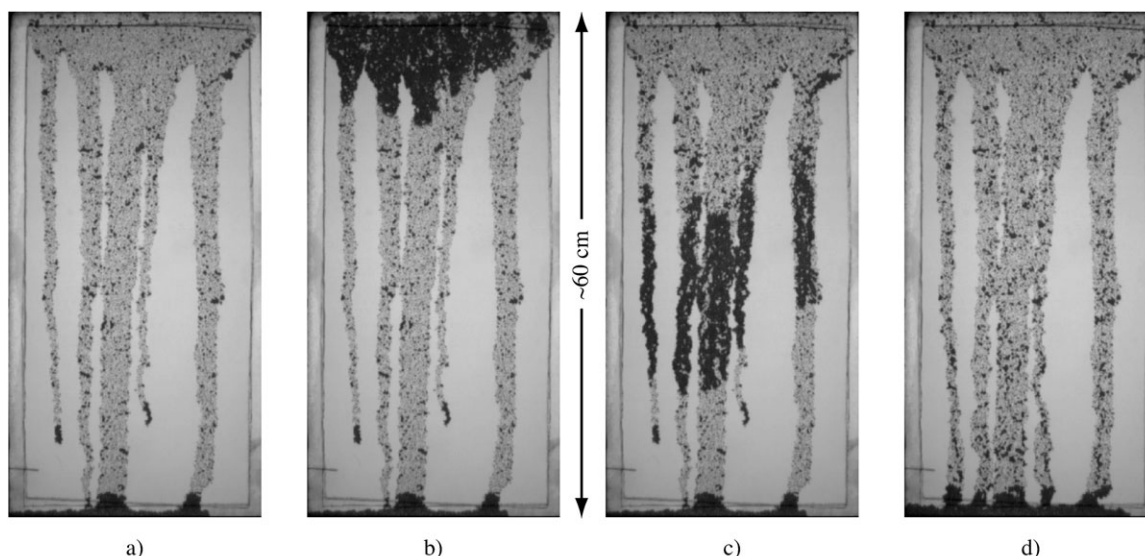


**Fig. 9.** Influence of previous events on formation of gravity-driven fingers at  $\cos\theta = 1.0$ .

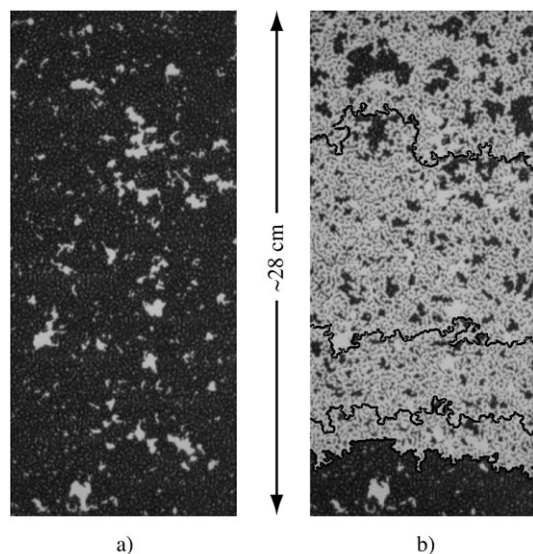


**Fig. 10. Relationship between residual moisture and  $\cos\theta$ .** (a) Saturated condition produced by slow horizontal displacement of air by water in our 15- by 30-cm cell; dark regions are water-filled, light regions air-filled. (b) We then successively tilted the cell to inclinations of 75.5, 60, 41.4, and 0° from vertical. At each step we allowed the cell to drain freely. Capillary fringe at the bottom shows fluid left behind after drainage at vertical ( $\cos\theta = 1.0$ ). Moving upward, the black wavy lines show position of the capillary fringe at  $\cos\theta = 0.75, 0.5$ , and  $0.25$ . Both the size of fluid blobs left behind and residual saturation increase as  $\cos\theta$  decreases.

and allowed gravity drainage to a residual moisture content. To drain the capillary fringe, we used absorbent towels to apply a gentle suction along the bottom boundary. At steep inclinations, this procedure produced a residual moisture structure that consisted of small disconnected fluid blobs distributed pretty much uniformly about the cell (Fig. 10). At lower inclinations, fluid blobs left behind after gravity drainage were generally larger and less uniform (shape, size, spatial distribution), leading to higher average residual moisture content.

Contrary to results in porous media, initial moisture appeared to enhance fingering relative to dry initial conditions. Figure 11 shows a typical experiment in which dyed water was ponded above a uniformly distributed initial moisture field of undyed water. Infiltration (Fig. 11a) entraps significant amounts of air to form a complicated front characterized by sharp, short wavelength perturbations. This contrasts significantly with the smoother, longer wavelength perturbations observed during infiltration into the same cell under dry initial conditions (Fig. 5a). Gravity-driven fingers form when fluid in the pond is exhausted and further advancement requires drainage along the trailing edge of the fluid slug (Fig. 11b). Fingers (Fig. 11c and 11d) form long, complicated structures that entrain significant amounts of air. With respect to dry initial conditions in the same cell, fingers appeared to be faster, longer, narrower, more complex, and more numerous. We also observed that the fingers tended to meander more on their way downward, merging with adjacent fingers and splitting into smaller fingers. In doing so, the advancing fingers leave little fluid behind. However, they do rearrange and interact with the initial moisture field. In Fig. 11, the dyed fluid in the fingers transitions from dark to shades of gray as it mixes with the undyed water used to create the initial moisture field.

### EXPERIMENTAL OBSERVATIONS: SINGLE FINGERS FROM POINT SOURCES

The number, size, and behavior of individual fingers initiated under redistribution were tied closely to the size of perturbations present at the onset of instability. To more clearly understand finger behavior, we generated individual fingers from the controlled perturbation produced by steady fluid supply to a point source at the top of the fracture. The supply rate was varied between experiments to alter viscous forces, and fracture inclina-

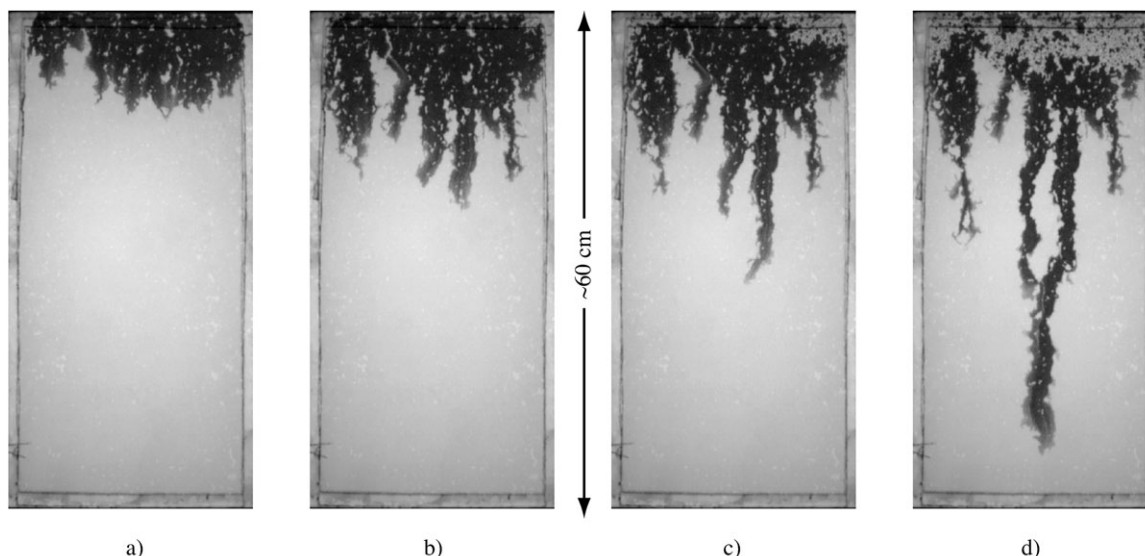


**Fig. 11. Formation of gravity-driven fingers following ponded infiltration ( $V_p = 6.98 \text{ cm}^3$ ) into a uniform initial moisture field at  $\cos\theta = 0.25$ .** Water in the initial moisture field was not dyed, and is nearly transparent.



tion was changed to control gravity forces. To begin this section, we consider infiltration into a dry fracture. We then look at the influence of initial moisture.

### Initially Dry Fractures

We conducted 76 experiments in which individual fingers were generated from steady supply to a point source at the top of a dry fracture. To improve image resolution, experiments were conducted in the 15- by 30-cm cell ( $\approx 10 \text{ cm}^3$  aperture volume). Four values of  $\cos\theta$  were considered (1.0, 0.5, 0.25, and 0.125). Supply rate,  $Q$  ( $\text{L}^3 \text{ T}^{-1}$ ), was varied over a range from 0.022 to  $13.3 \text{ cm}^3 \text{ min}^{-1}$ . The cell was disassembled, cleaned, dried, and reassembled between trials.

At low  $Q$ , infiltration from a point source at the top of a vertical fracture is initially pinned to the upper boundary by capillary forces (Fig. 12a). The finger grows preferentially in the direction of gravity and eventually reaches sufficient length to break free of the top boundary and move on its own. The size of this initial fingertip is controlled by the balance between capillary, gravitational, and viscous forces rather than an initial perturbation; otherwise it is directly analogous to those seen in the redistribution experiments. The saturated fingertip is separated from the fluid source by a partially desaturated zone (Fig. 12b). Fluid structure within the desaturated zone results from a combination of drainage behind the saturated fingertip and resupply from the fluid source. Fluid from the source continues to move through the desaturated zone to resupply the fingertip, which loses fluid as it wets the fracture behind it (Fig. 12c and 12d). At low  $Q$  and large  $\cos\theta$ , connection between the fingertip and the fluid source was intermittent. Flow from the source would follow behind the tip, reconnect when the tip slowed due to fluid loss, and disconnect again when the fingertip was replenished.

The influence of  $\cos\theta$  on finger behavior at low  $Q$  is

shown as Fig. 13. At  $\cos\theta = 1.0$  the finger is narrow, closely aligned with the gravitational vector, and exhibits substantial desaturation behind a saturated tip that is fully disconnected from the fluid source (Fig. 13a). Desaturation behind the fingertip decreases and connection to the fluid source increases as  $\cos\theta$  is reduced (Fig. 13b–13d). Fingers also become wider and slower, and the saturated tip is longer. Fingers meandered more at lower  $\cos\theta$ , where the increased importance of capillary fingering leads to a rougher and more complex structure that entraps air within the finger (Fig. 13c and 13d). It is important to note that gravity-driven fingering is an important process even at small fracture inclinations. Comparison of Fig. 13d and Fig. 14 clearly shows that infiltration at  $\cos\theta = 0.125$  ( $82.9^\circ$  from vertical) is very different than horizontal imbibition ( $\cos\theta = 0$ ).

The effects of  $Q$  on finger behavior at  $\cos\theta = 1.0$  are illustrated in Fig. 15. Desaturation behind the fingertip was small at large  $Q$  (Fig. 15a) and increased dramatically as  $Q$  was decreased (Fig. 15b–15d). Fingertips became narrower, shorter, and slower with decreasing  $Q$ . They also tended to meander more in response to local heterogeneity, and exhibit a more complicated outline than at large  $Q$ . Flow within the desaturated zone becomes more complex at lower values of  $Q$ , with continuous flow along narrow channels (Fig. 15c) replaced by a dripping mechanism that intermittently connects multiple pools (Fig. 15d). The increased dynamics associated with intermittent flow structures can lead to switching between pathways and the formation of dendritic secondary fingers (see Fig. 15d).

In our system, local aperture variability (i.e.,  $r_1$  curvature) subjects fingertips to finite amplitude perturbations at wavelengths on the order of the aperture spatial correlation length,  $\lambda$ . Figure 13d shows the effects of such a perturbation on a fingertip at small  $\cos\theta$ . After bifurcating, both tips advanced in parallel, then rejoined to entrap a blob of air. At steeper inclinations, we observed bifurcations in which one finger clearly domi-

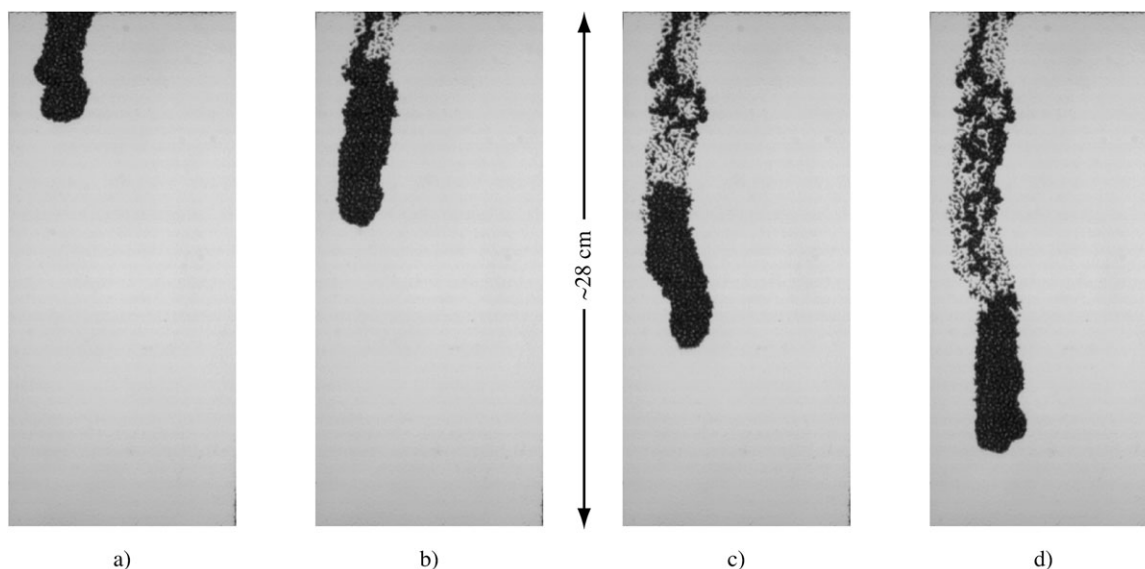
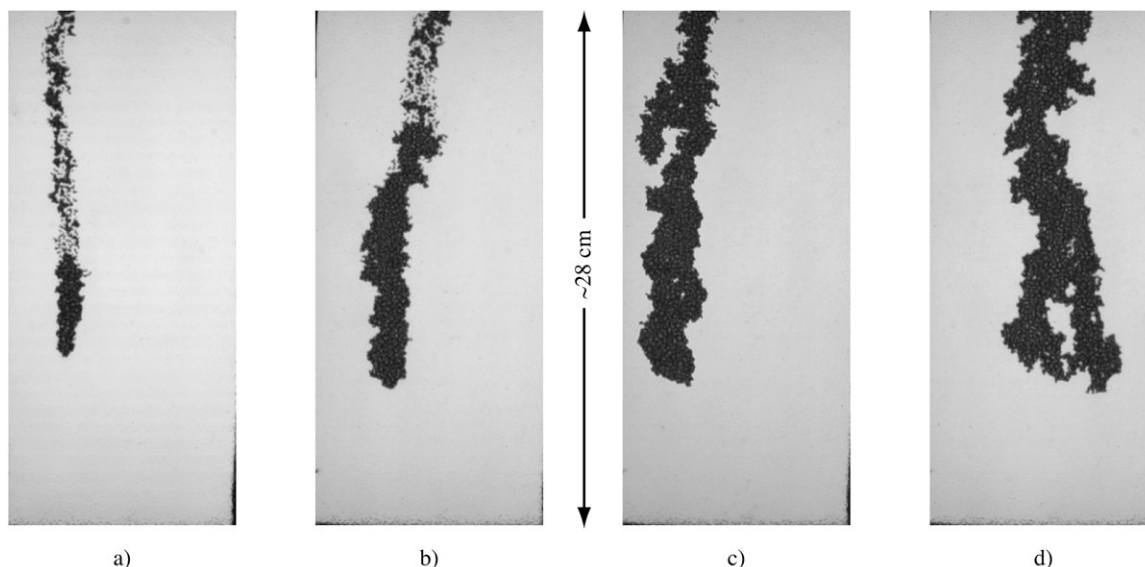


Fig. 12. Formation of a gravity-driven finger from steady supply ( $Q = 1.36 \text{ cm}^3 \text{ min}^{-1}$ ) to a point source at  $\cos\theta = 1.0$ .



**Fig. 13.** Effects of  $\cos\theta$  on finger behavior. Experiments were run at different  $\cos\theta$  values, but similar  $Q$ . Image times give an indication of relative velocity. (a)  $\cos\theta = 1.0$ ,  $Q = 0.254 \text{ cm}^3 \text{ min}^{-1}$ ,  $t = 90 \text{ s}$ ; (b)  $\cos\theta = 0.50$ ,  $Q = 0.265 \text{ cm}^3 \text{ min}^{-1}$ ,  $t = 200 \text{ s}$ ; (c)  $\cos\theta = 0.25$ ,  $Q = 0.247 \text{ cm}^3 \text{ min}^{-1}$ ,  $t = 285 \text{ s}$ ; and (d)  $\cos\theta = 0.125$ ,  $Q = 0.235 \text{ cm}^3 \text{ min}^{-1}$ ,  $t = 375 \text{ s}$ .

nated (Fig. 16). A finite amplitude perturbation splits the fingertip (Fig. 16a) to form two distinct tips that continue downward and compete for the available fluid (Fig. 16b). Capillary and gravity forces favor growth of the most advanced fingertip (Fig. 16c). Eventually, the

dominant finger starves the other and continues to advance. The failed bifurcation is left behind as a saturated lobe on the side of the moisture structure (Fig. 16d). Dendritic secondary fingers commonly developed from such appendages to the moisture structure (Fig. 17). Shortly after the initial bifurcation (Fig. 17a), the more advanced fingertip dominates, while the smaller fingertip is left behind as an appendage to the moisture structure (Fig. 17b). Later, flow through the desaturated zone joins with this appendage (Fig. 17c) to form a second, dendritic finger (Fig. 17d).

Where flow within the desaturated zone became disconnected, small fluid blobs were pinned within the aperture field by capillary forces. Individual blobs would grow in size as fluid was added. The stored fluid is eventually released as a discrete pulse. Figure 18a shows a poorly connected desaturated zone that turned steady supply from above into intermittent drips. To examine temporal behavior at a single fluid blob (Fig. 18b), we measured changes between rapidly collected sequential images. In Fig. 18c, white zones repeatedly drained and filled, while the rest (black) remained unchanged. Beyond simple pulsation, this system exhibits a potential for highly complicated behavior, particularly if one considers hysteresis, viscous energy loss during discharge, and dynamic contact angle. As such, it bears a strong resemblance to the “dripping faucet” problem considered by Shaw (1984), where nonlinear coupling between state variables leads to a rich variety of behavior from steady to chaotic. Beyond the scale of a single fluid blob, it may be possible for fluid cascades to rapidly span the system. Finally, the example shown in Fig. 18 exhibited pulsation along a single pathway; however, we also noted pulsed flow to switch pathways within the desaturated zone as connections snapped and reformed (Fig. 19). Such small-scale reconfigurations can lead to the formation of macroscopic dendrites as seen in Fig. 15d.

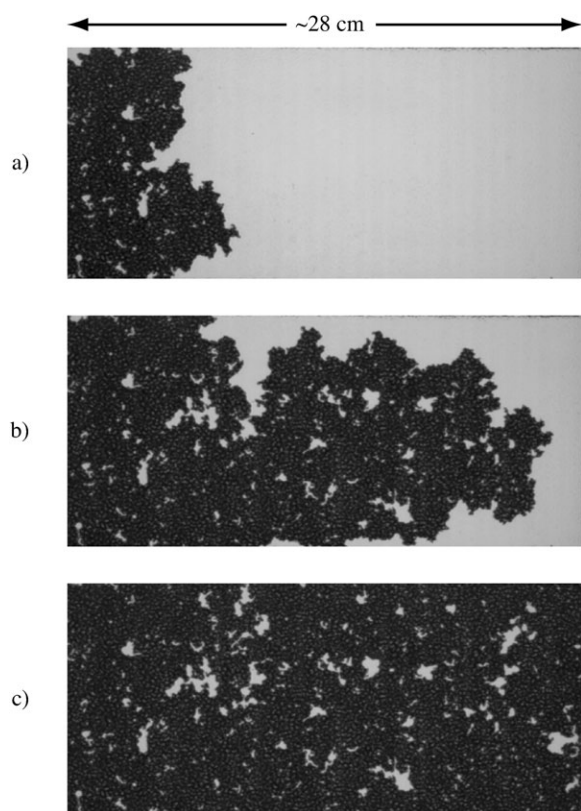


**Fig. 14.** (a, b) Slow horizontal ( $\cos\theta = 0.0$ ) invasion of the air-filled 15- by 30-cm cell. Invasion is completely controlled by capillary forces (quasistatic displacement), (c) eventually filling the cell to a saturated condition where air is fully entrapped at a variety of length scales.

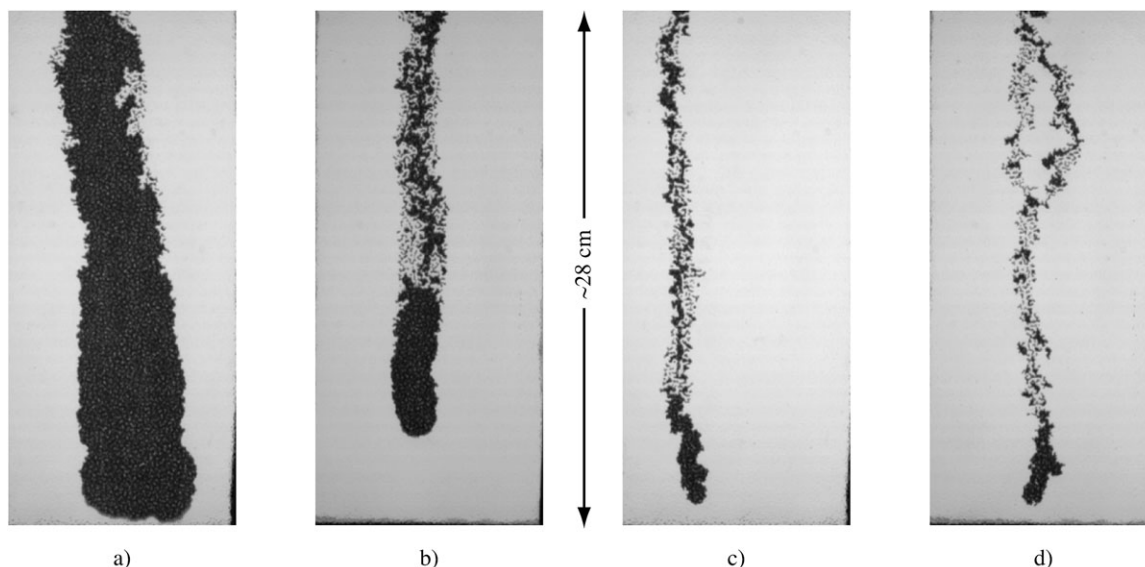


Fig. 15. Effect of  $Q$  on finger behavior under dry initial conditions at  $\cos\theta = 1.0$ . Image times give an indication of relative velocity. (a)  $Q = 13.3 \text{ cm}^3 \text{ min}^{-1}$ ,  $t = 32 \text{ s}$ ; (b)  $Q = 1.25 \text{ cm}^3 \text{ min}^{-1}$ ,  $t = 36 \text{ s}$ ; (c)  $Q = 0.254 \text{ cm}^3 \text{ min}^{-1}$ ,  $t = 108 \text{ s}$ ; and (d)  $Q = 0.0243 \text{ cm}^3 \text{ min}^{-1}$ ,  $t = 690 \text{ s}$ .

### Influence of Initial Moisture

To explore the influence of initial moisture on fingers formed by steady supply to a point source, we conducted one experiment in a structured moisture field, then moved on to systematic experimentation in uniform initial moisture fields (27 experiments). Experiments were conducted at  $\cos\theta = 1.0, 0.75, 0.5$ , and  $0.25$ ;  $Q$  was varied over a range from  $0.35$  to  $2.5 \text{ cm}^3 \text{ min}^{-1}$ . Experiments were performed in the  $30 \times 60 \text{ cm}$  cell ( $\approx 41\text{-cm}^3$  aperture volume) to allow sufficient room for fingers to interact with the in situ moisture field.

We began with an experiment designed to determine if steady supply from a point source would follow an existing moisture structure. To create the structured moisture field outlined in Fig. 20a, we inverted the cell slightly and imbibed undyed water. The apparatus was

then quickly rotated to  $\cos\theta = 0.25$ , placing the imbibed water at the top of an otherwise dry fracture. Immediate redistribution of the imbibed water led to the formation of one large finger, which wetted the outlined zone as it passed through. Subsequent steady flow from a point source formed a near vertical finger in the uniformly distributed portion of the initial moisture field, then diverted laterally to stay within that field (Fig. 20b and 20c). The finger follows a narrow and complicated pathway that abruptly widens near the bottom as it enters the saturated capillary fringe left behind by the previous event (Fig. 20c). Accumulation of fluid above a lobe in the initial moisture field (Fig. 20b and 20c) led to a new dendritic finger that invaded the dry region beneath (Fig. 20d). In time, all flow switched into the new finger (Fig. 21a), providing an excellent opportunity to observe

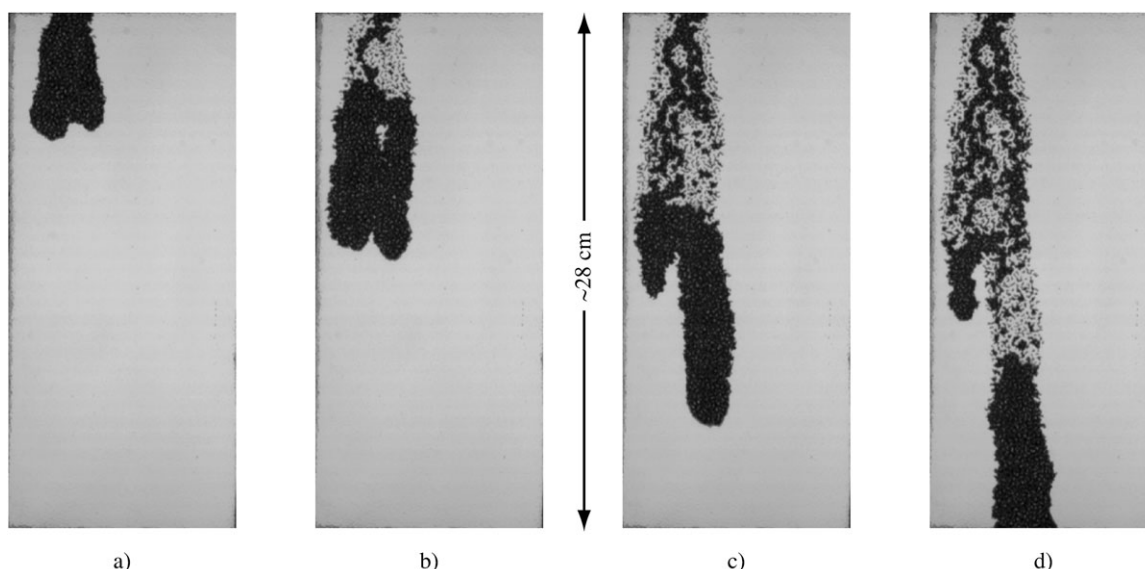
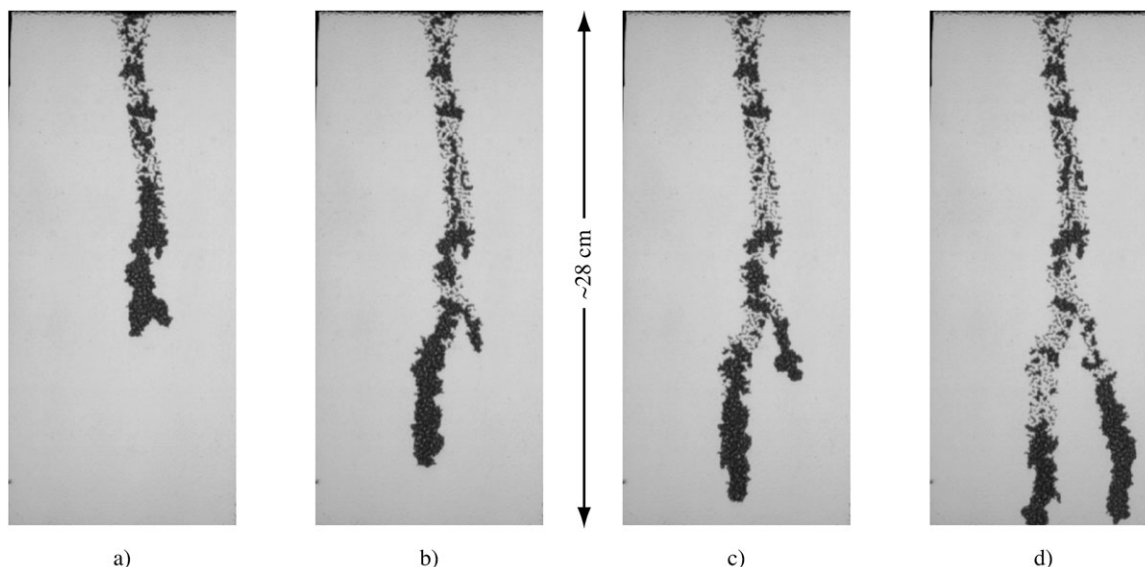


Fig. 16. Macroscopic instability of a gravity-driven finger initiated by steady supply ( $Q = 2.51 \text{ cm}^3 \text{ min}^{-1}$ ) to point source at the top of the 15-by 30-cm air-filled cell at  $\cos\theta = 1.0$ .





**Fig. 17.** Dendritic secondary finger formed in the 15- by 30-cm cell ( $\cos\theta = 0.50$ ) from steady supply ( $Q = 0.0254 \text{ cm}^3 \text{ min}^{-1}$ ) under dry initial conditions.

the difference between dry and prewetted initial conditions. As seen in Fig. 21b, the area swept by the finger on the left (prewetted zone) exhibits a structure very similar to what we see in the desaturated zone behind a fingertip in an initially dry fracture. It is much narrower and more complicated than the relatively wide and smooth region swept by the finger to the right (initially dry zone).

By focusing on a single finger (Fig. 20), we were able to observe how it interacted with the initial moisture field. When an advancing fingertip contacts the meniscus surrounding an in situ blob of fluid, the two join, changing the shape of the fingertip and altering the local balance between capillary, viscous, and gravitational forces. This mechanism may explain the apparent con-

tradiction between our observation that initial moisture has a destabilizing influence and results from granular porous media that attribute a stabilizing influence to initial moisture (Diment and Watson, 1985; Glass and Nicholl, 1996; Wang et al., 2003a, 2003b). In granular porous media, wetting fluid is expected to be found as pendular rings at each intergranular contact point, and may also be present as films on the micro-rough surfaces of grains. Both pendular rings and films will enhance spreading of the wetting fluid and thus suppress the formation of fingers. In our system, the initial moisture field is discontinuous, such that local water saturation is either 0 or 100%. Discrete blobs of water are separated by air-filled regions that do not support a water film. The discrete blobs impose sudden perturbations

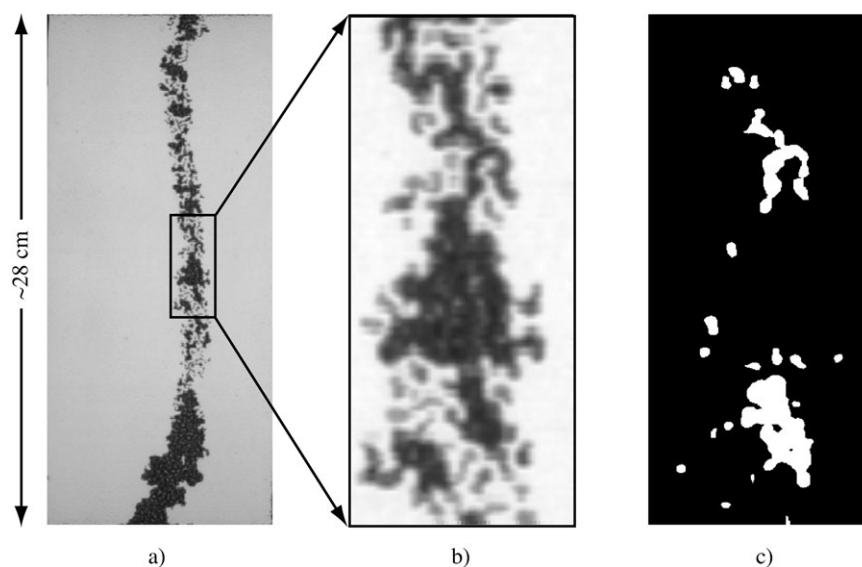


**Fig. 18.** Unsteady flow resulting from steady supply to an inclined fracture. (a) Desaturated zone behind a fingertip in the 15- by 30-cm cell at steady supply ( $Q = 0.025 \text{ cm}^3 \text{ min}^{-1}$ ) under dry initial conditions ( $\cos\theta = 0.50$ ). (b) Enlargement of the boxed area focuses on a single fluid blob. (c) Dynamic behavior within the boxed area is explored by recording changes in saturation with time. White represents repeated drain and fill cycles (e.g., drip points), while black indicates no change.

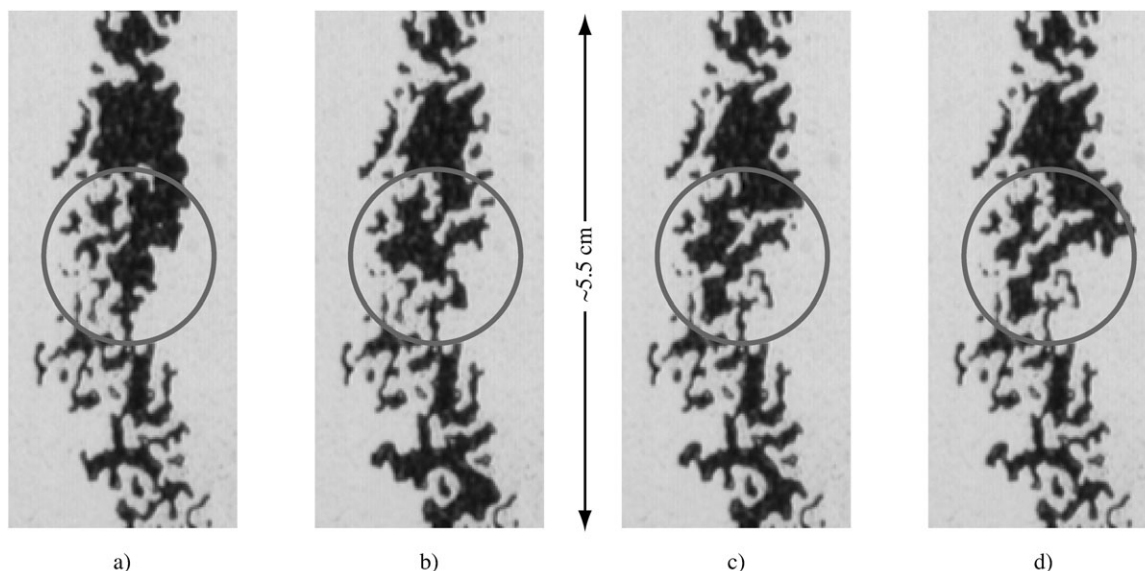


Fig. 19. Four different fluid configurations observed within the desaturated zone behind a finger formed from steady supply ( $Q = 0.0198 \text{ cm}^3 \text{ min}^{-1}$ ) to a point source. As illustrated in these enlargements, pulsed flow imposed by the desaturated zone led to changes in connection.

to infiltration that tend to break up a front and focus fingers.

Fingers in uniformly distributed initial moisture fields were observed to be narrower and faster than for dry initial conditions. We also observed fingertips to experience sudden lateral diversions and extensive splitting. In the uniform fields, fingers are repeatedly subjected to perturbations by contacting in situ blobs. Such perturbations appear to exert a first-order control on finger behavior. Repeated perturbations at a given scale controls finger width, while the details of the initial moisture field may cause the fingertip to split, merge, and/or be diverted. Figure 22a shows two experiments, one completed and one in progress. In the experiment shown on the left, a finger split into multiple fingers in a uniform initial moisture field. The second experiment, shown on the right, began as a single finger (Fig. 22a), then

contacted two large blobs (marked by the ellipse) and split (Fig. 22b). The finger split again and rejoined within the circled region (Fig. 22c). As the finger proceeded it continued to interact with the in situ fluid blobs; splitting, merging, and joining with a remnant of the previous experiment (Fig. 22d). In each of the images, fingertips are a medium shade of gray, illustrating mixing between the in situ fluids (lightly dyed) and advancing fingers (heavily dyed).

### QUANTITATIVE EVALUATION OF FINGER BEHAVIOR

Our experimental matrix varied viscous and gravitational forces (i.e., fluid supply and  $\cos\theta$ ) for two different unstable boundary conditions, redistribution following ponded infiltration and single fingers from a point source.

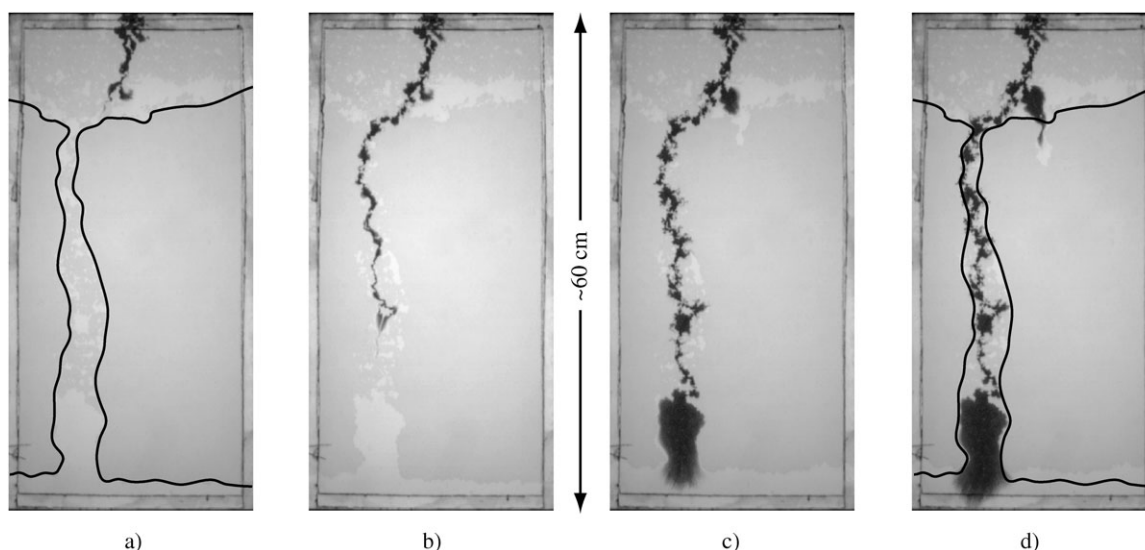
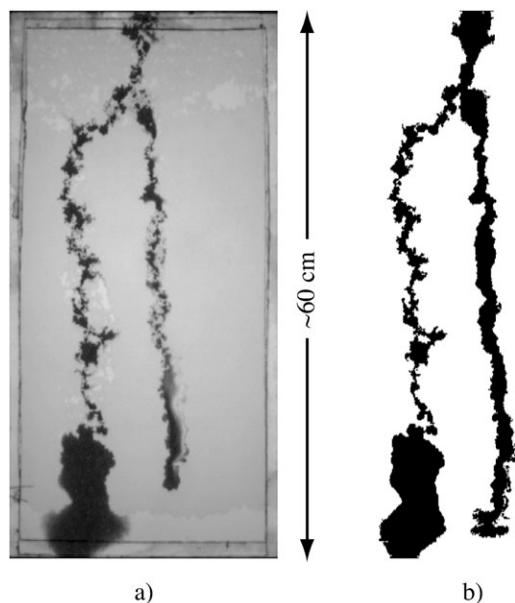


Fig. 20. Steady supply from a point source ( $Q = 0.0639 \text{ cm}^3 \text{ min}^{-1}$ ) into a structured initial moisture field in the 30- by 60-cm cell at  $\cos\theta = 0.25$ . The initial moisture field (clear water) is outlined in (a) and (d).



**Fig. 21.** Comparison of fingers formed under wet and dry initial conditions. (a) Finger to the left followed an existing moisture field, while the one to right invaded the dry portion of the aperture field (see Fig. 20). (b) Binary image marking the area swept by each finger.

Wherever possible, we obtained quantitative data on finger width, velocity, and tip length. To best illustrate the influence of viscous and gravitational forces, we present raw data from the more extensive data sets obtained under dry initial conditions. Then, we employed a simple scale analysis to develop relations between the measured variables. The simple models allowed us to collapse the data and compare measurements obtained under different boundary and initial conditions.

### Measured Data

Quantitative data were extracted from digital images acquired at regular intervals in each experiment. All

measurements were referenced to the gravitational vector (i.e., the component of gravity in the plane of the fracture). Fingertip length,  $L_{tip}$ , was defined as the distance between the apex of the fingertip and the trailing edge, as measured along the gravitational vector. Finger velocity,  $v$  ( $L T^{-1}$ ), was taken to be the rate of translation of the fingertip along the gravitational vector. Finger width,  $W$  ( $L$ ), was defined as the width of the pathway wetted by the finger as it crosses the fracture, and measured perpendicular to the gravitational vector. Because these quantities varied as fingers traversed the cell, we report averages taken across the largest travel distance possible.

### Redistribution Following Pondered Infiltration

Many of the redistribution experiments produced multiple fingers; for measurement purposes we treated each finger individually. For analysis, we define the infiltration depth,  $L_i$  ( $L$ ), as  $V_p$  divided by the product of  $\langle a \rangle$  and fracture width. In effect,  $L_i$  represents the depth to which a given volume would penetrate our fracture as a perfectly flat front. Measured fingertip lengths show a strong positive correlation to  $L_i$ , (Fig. 23), with most of the data plotting above the 1:1 line given by  $L_{tip} = L_i$ . Conversely,  $L_i$  is only weakly dependent on  $\cos\theta$ . The velocity of individual fingers is shown as a function of  $L_i$  as Fig. 24. Despite significant scatter, data show a strong positive correlation to  $\cos\theta$ , and increases with  $L_i$  at  $\cos\theta = 0.50, 0.75$ , and  $1.0$ .

Measured finger widths (Fig. 25) show a strong positive correlation to  $L_i$  and appear to be independent of  $\cos\theta$  except at the largest values of  $L_i$ . The apparent correlation between  $W$  and  $\cos\theta$  at large  $L_i$  is an artifact of the limited fracture length. The solid line shown in Fig. 25 represents  $\lambda_m/2$  from Eq. [9], which predicts the fastest growing wavelength from a flat displacement front in a Hele-Shaw cell. To apply this relation, we use Eq. [10] to estimate velocity from  $L_i$ ;  $(\psi_w - \psi_d)$  was

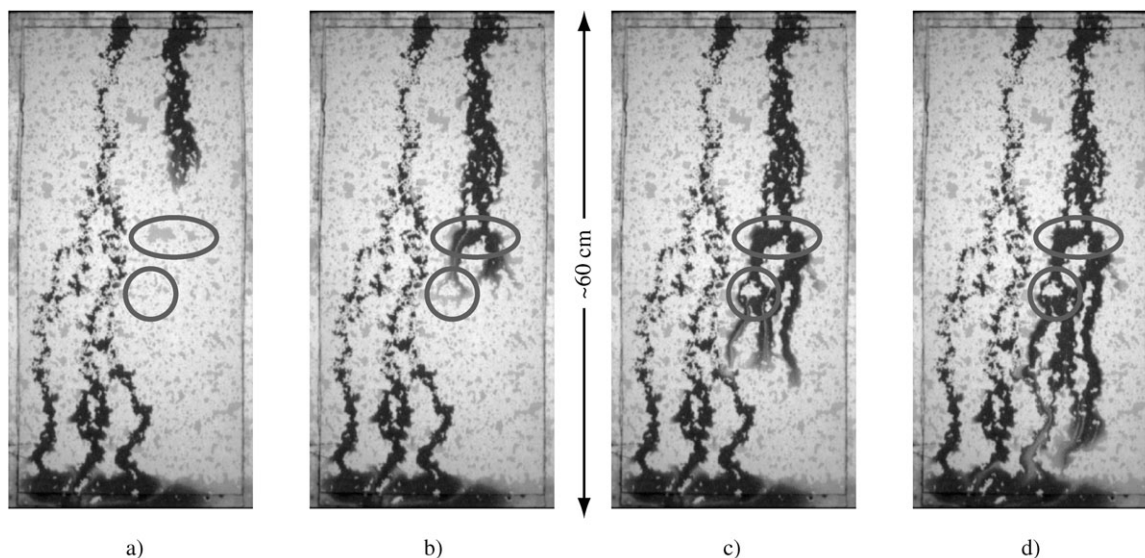


**Fig. 22.** Finger splitting in a uniform initial moisture field. The 30- by 60-cm cell was saturated, then drained to residual moisture content at  $\cos\theta = 0.25$ . Steady supply ( $1.79 \text{ cm}^3 \text{ min}^{-1}$ ) was applied from a point source located to the right of center.



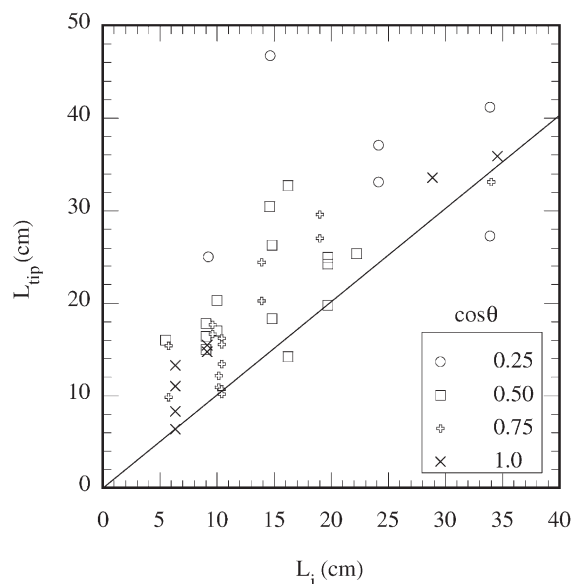


**Fig. 23.** The length of individual fingertips ( $L_{tip}$ ) in the redistribution experiments are shown as a function of infiltration length ( $L_i$ ) for experiments run under dry initial conditions.

taken to be 2.85 cm (Table 1). Almost all of the data plot above the Hele-Shaw prediction; the others correspond to fingers that lost fluid to their larger siblings. Results suggest that measured data reflect the formation of fingers from finite-amplitude perturbations rather than the infinitesimal perturbations at all wavelengths assumed in Eq. [9]; however, Eq. [9] may act as an approximate lower bound on finger width. Damping of initial perturbations and hence increased finger width is expected to be mostly dependent on  $L_i$ , little dependence on  $\cos\theta$  is expected or observed.

### Single Fingers from Point Sources

Single fingers were generated from steady supply to a point source. The supply rate ( $Q$ ) was varied over a

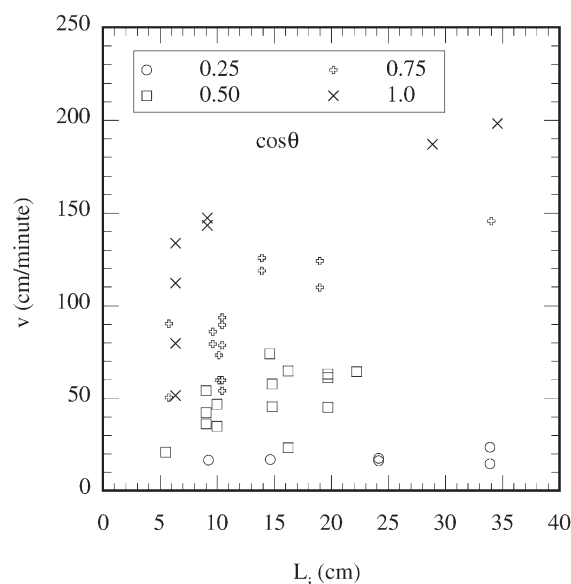


**Fig. 24.** The average velocity ( $v$ ) of individual fingers in the redistribution experiments are shown as a function of infiltration length ( $L_i$ ) for experiments run under dry initial conditions.

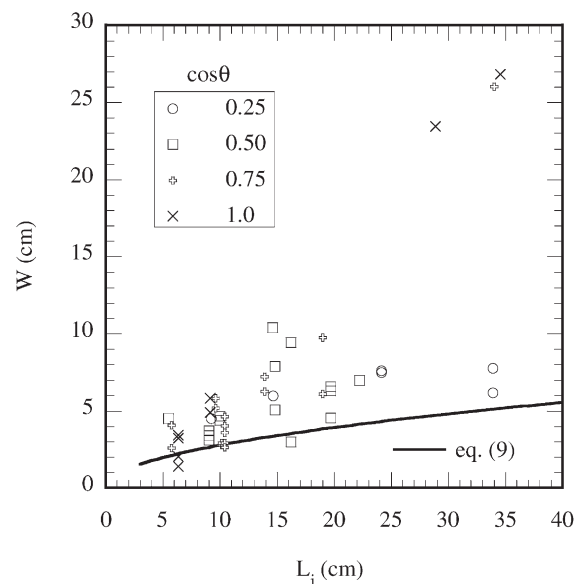


**Fig. 25.** The average width ( $W$ ) of individual fingers in the redistribution experiments are shown as a function of infiltration length ( $L_i$ ) for experiments run under dry initial conditions. The solid line represents  $\lambda_m/2$  from Eq. [9].

range of more than three orders of magnitude, and is therefore plotted on log scale. Fingertip length was only measured for fingers where desaturation occurred behind the fingertip, which was not observed at small  $\cos\theta$  or large  $Q$ . Measured data (Fig. 26) show that tip length decreases with  $\cos\theta$  and increases with  $Q$  along well-defined paths. This result contrasts with the redistribution experiments, where only a weak correlation to  $\cos\theta$  was observed. Note also the reduced scatter. Finger velocity increases with both  $Q$  and  $\cos\theta$  (Fig. 27), following approximately parallel paths across a wide range of  $Q$ . Finger width also plots along four separate paths (Fig. 28) that decrease with increasing  $\cos\theta$ . Along each

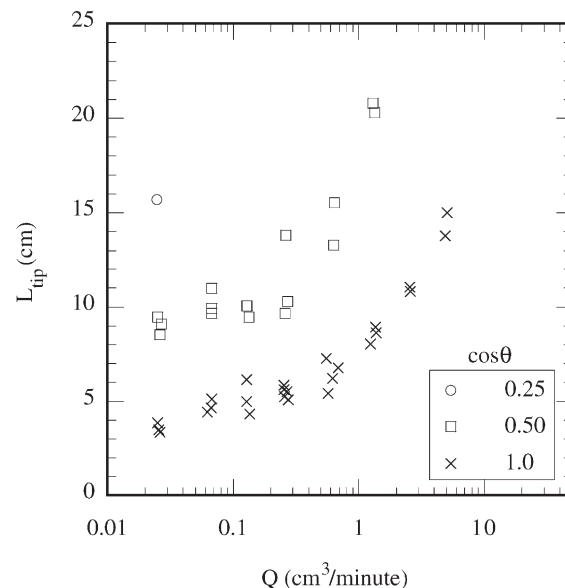


**Fig. 26.** The length of individual fingertips ( $L_{tip}$ ) initiated from a point source are shown as a function of supply rate ( $Q$ ) for experiments run under dry initial conditions.

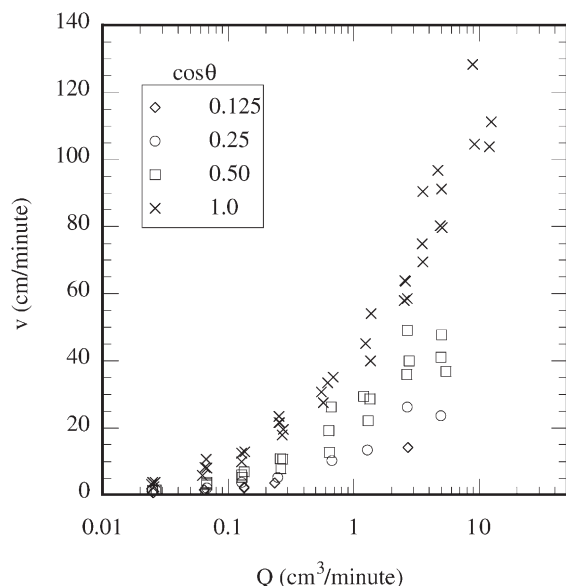


Fig. 27. The average velocity ( $v$ ) of individual fingers initiated from a point source are shown as a function of supply rate ( $Q$ ) for experiments run under dry initial conditions.

of the four paths finger width increases gradually at small  $Q$ , then experiences a rapid increase at larger  $Q$ .

### Scale Analysis

In our experiments, the principal length scales associated with dynamic structure are fingertip length and finger width. A simple local scale analysis is used to develop approximate relations for those parameters as functions of finger velocity. In our scale analysis, we assume that inertial forces are negligible (Darcian flow) and express the local balance between gravity, viscous, and capillary forces in terms of local pressure differentials,  $\Delta P_i$  ( $F L^{-2}$ ), where

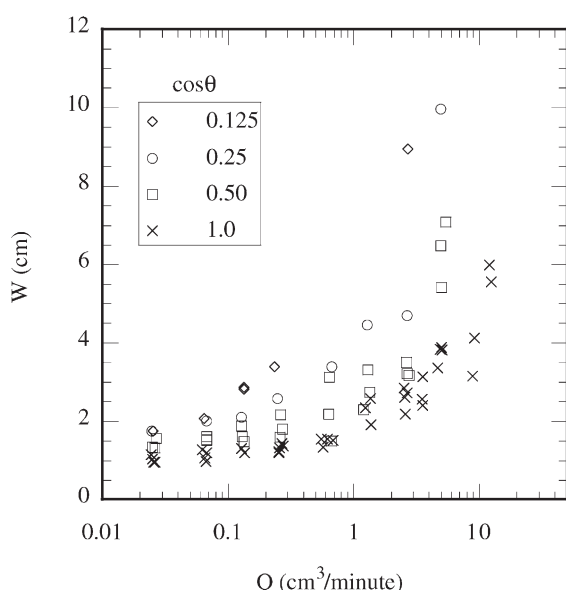


Fig. 28. The average width ( $W$ ) of individual fingers initiated from a point source are shown as a function of supply rate ( $Q$ ) for experiments run under dry initial conditions.

$$\Delta P_g + \Delta P_v + \Delta P_c = 0 \quad [11]$$

The sign of each  $\Delta P_i$  in Eq. [11] depends on its local action with respect to the situation of interest. We begin with definitions for the  $\Delta P_i$ , then consider the tip length at which a finger becomes stagnant (i.e., ceases motion). Next, we develop relations for fingertip length and width as a function of velocity; for both, we compare predictions to experimental measurements. We conclude this section by exploring the importance of dynamic capillary pressure in the context of our scale analysis and experimental data.

### Pressure Differentials

Consider a finger within an otherwise air-filled fracture (Fig. 29). The fracture is assumed to have impermeable walls that are water-wettable and to be inclined from vertical by an angle of  $\theta$ . We assume that each fluid is individually homogenous and that interfaces between the two extend from one solid surface to the other (i.e., no encapsulation or film flow). The air phase is taken to be in viscous and free to escape through the edges of the system. Under these conditions, and in lieu of any external applied fluid pressure, flow will be controlled by gravitational, capillary, and viscous forces within the water phase. The local pressure differential associated with gravitational forces may be approximated as

$$\Delta P_g \approx \Delta \rho g \cos \theta h_g \quad [12]$$

where  $h_g$  is the local gravitational length scale of interest. For viscous forces we have

$$\Delta P_v \approx v' \mu h_v (k k_r)^{-1} \quad [13]$$

where  $h_v$  reflects the local viscous length scale and  $v'$  represents local fluid velocity ( $L T^{-1}$ ). Given that capil-

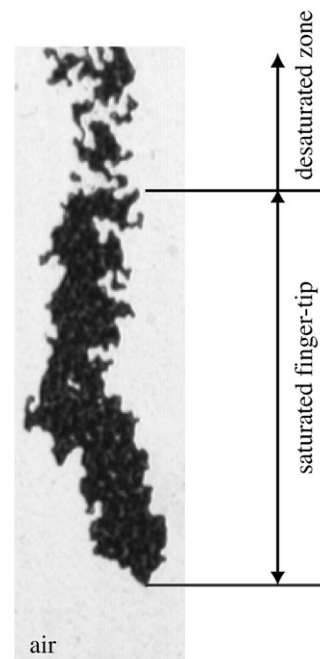


Fig. 29. Saturated fingertip and desaturated zone in an otherwise air-filled fracture.

lary pressure will vary along the air–water interface, the pressure differential between any two locations within the water phase may be approximated as

$$\Delta P_c \approx \sigma[(r_1^{-1} + r_2^{-1})_A - (r_1^{-1} + r_2^{-1})_B] \quad [14]$$

where subscripts “A” and “B” denote two arbitrary locations along the air–water interface. For completeness, we note that dimensionless parameters traditionally considered to govern system behavior (e.g., capillary and bond numbers) are in effect, ratios of the  $\Delta P_i$ . However, to our knowledge, the representation of capillary variability in Eq. [14] is different from what has been used in the past.

### Stagnant Fingertip Length

If a disconnected fingertip is at rest, then  $\Delta P_v = 0$  and capillary forces must balance gravity:

$$\Delta P_g - \Delta P_c = 0 \quad [15]$$

Insertion of Eq. [12] and Eq. [14] into Eq. [15] leads to

$$\Delta \rho g \cos \theta h_g = \sigma[(r_1^{-1} + r_2^{-1})_A - (r_1^{-1} + r_2^{-1})_B] \quad [16]$$

We take location A as the leading edge of the stagnant fingertip and location B as the trailing edge; thus,  $h_g = L_{\text{tip}}$ . To solve Eq. [16] for  $L_{\text{tip}}$ , we would need representative values of  $r_1$  and  $r_2$  at both locations. As these are unknown, we assume that pressure head along the leading edge of the finger, location A, may be approximated by  $\psi_w$ . Likewise, we assume that pressure head along the trailing edge of the finger, location B, may be approximated by  $\psi_d$ . Implementation of these assumptions gives

$$L_{\text{tip}} = (\psi_w - \psi_d) / \cos \theta \quad [17]$$

Measured values of  $\psi_w$  and  $\psi_d$  (see Table 1) lead to an estimate of 2.85 cm for  $L_{\text{tip}}$  at  $\cos \theta = 1.0$ , which compares well with measured values ( $L_{\text{tip}} = 2.2 - 2.7$  cm) for fingers that stalled within the fracture at  $\cos \theta = 1$ .

### Fingertip Length as a Function of Finger Velocity

If the fingertip is in motion, viscous forces and capillary forces act against gravity, and Eq. [11] may be written as

$$\Delta P_g - \Delta P_c - \Delta P_v = 0 \quad [18]$$

Again, we assume that capillary pressures along the leading and trailing edges of the finger may be represented by  $\psi_w$  and  $\psi_d$ , respectively. Then, insertion of Eq. [12], [13], and [14] into Eq. [18] gives

$$\Delta \rho g \cos \theta h_g - \left( \Delta \rho g (\psi_w - \psi_d) + \frac{v' \mu h_v}{k k_r} \right) = 0 \quad [19]$$

For our situation,  $h_g = h_v = L_{\text{tip}}$ ; thus, rearrangement of Eq. [19] leads to

$$L_{\text{tip}} = \frac{(\psi_w - \psi_d)}{\cos \theta} \left( 1 - \frac{v'}{K_s k_r \cos \theta} \right)^{-1} \quad [20]$$

From Eq. [20],  $L_{\text{tip}}$  becomes infinite as  $v' \rightarrow K_s k_r \cos \theta$ . Note also that Eq. [20] collapses to Eq. [17] at  $v = 0$ .

We measured  $L_{\text{tip}}$  on disconnected fingers formed un-

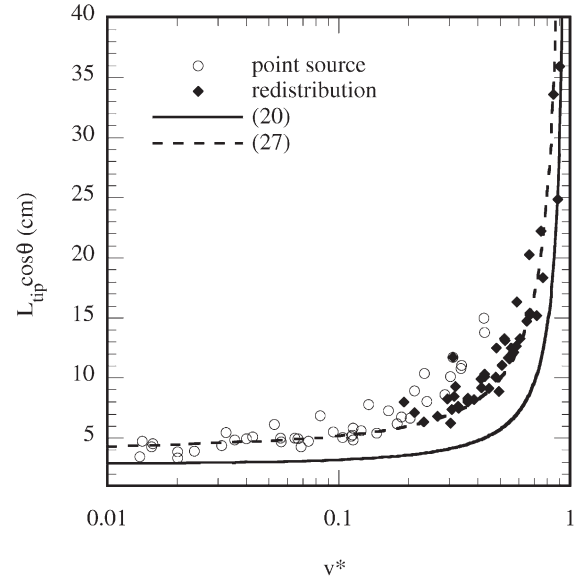


Fig. 30. Scaled finger tip length ( $L_{\text{tip}} \cos \theta$ ) is shown as a function of scaled finger velocity ( $v^* = v / K_s k_r \cos \theta$ ). Data from both the redistribution and point source experiments under dry initial conditions are shown, along with two simple models representing Eq. [20] and [27].

der dry initial conditions for both redistribution and point source boundary conditions. For consistency with Eq. [20], we plotted  $L_{\text{tip}} \cos \theta$  as a function of scaled finger velocity ( $v^* = v / K_s k_r \cos \theta$ ) as Fig. 30. Because fingertips were essentially saturated, we set  $k_r = 1$ . The solid line represents Eq. [20], with  $(\psi_w - \psi_d)$  approximated by the difference between wetting and drainage pressures (2.85 cm). Data from both experimental sets collapse to plot on a single curve. The simple model suggested by Eq. [20] fits the data at large  $v^*$ , but underestimates measured values for the rest of the range. The discrepancies are most pronounced at intermediate values of  $v^*$ .

### Finger Width as a Function of Finger Velocity

To consider finger width, we focus on active growth along the leading edge of the fingertip. In a Hele-Shaw cell, fingers transition from nearly flat sides into a smoothly rounded tip. The same basic structure is expected in a variable-aperture field, with the addition of aperture induced irregularities along the interface (Fig. 29). Within this region,  $\Delta P_c$  along the rounded fingertip works to widen the finger, while the difference between gravity and viscous forces ( $\Delta P_g - \Delta P_v$ ) pulls it downward. Thus, the resulting balance equation is again given by Eq. [18], but with a different representation of the various  $\Delta P_i$ s. Fingertip growth occurs within the radius of the fingertip (i.e., a distance of about  $W/2$  from the finger apex). Thus, the representative length scale for  $h_g$  and  $h_v$  is taken to be approximately  $W/2$ . For  $\Delta P_c$  we are interested in locations at the apex of the fingertip (Location A) and where the fingertip transitions into the flat finger sides (Location B). With these definitions, insertion of Eq. [12], [13], and [14] into Eq. [18] gives

$$\frac{\Delta \rho g \cos \theta W}{2} - \sigma[(r_1^{-1} + r_2^{-1})_{\text{apex}} - (r_1^{-1} + r_2^{-1})_{\text{side}}] -$$



$$\frac{v' \mu W}{2k k_r} = 0 \quad [21]$$

Solving for  $W$  yields

$$W = \frac{2\sigma[(r_1^{-1} + r_2^{-1})_{\text{apex}} - (r_1^{-1} + r_2^{-1})_{\text{side}}]}{\Delta \rho g \cos \theta} \left(1 - \frac{v'}{K_s k_r \cos \theta}\right)^{-1} \quad [22]$$

Note that when  $r_1$  is referenced to within the finger, it will be negative for wetting displacement. In general, the influence of gravity acts as a siphon that causes apertures invaded above the apex of the finger to have on average a lower  $(r_1^{-1} + r_2^{-1})$ . Hence, the term  $[(r_1^{-1} + r_2^{-1})_{\text{apex}} - (r_1^{-1} + r_2^{-1})_{\text{side}}]$  in Eq. [22] will be positive.

To apply Eq. [22] we must understand how  $r_1$  and  $r_2$  will vary from point to point along the interface of a growing fingertip. Let us first consider two limiting situations: (i) where  $r_1$  can be neglected relative to  $r_2$  (a Hele-Shaw cell, large  $C/\delta$ ) and (ii) where  $r_2$  may be neglected relative to  $r_1$  (directional capillary fingering, small  $C/\delta$ ). Neglecting  $r_1$  ( $C/\delta$  large), we find the Hele-Shaw result by recognizing that  $(r_2)_{\text{side}} \rightarrow \infty$  as the tip transitions into the flat finger side. Thus, curvature of the interface is entirely determined by  $(r_2)_{\text{apex}}$ , which will be approximately  $W/2$ :

$$W = 2 \left( \frac{\sigma}{\Delta \rho g \cos \theta} \right)^{1/2} \left( 1 - \frac{v'}{K_s k_r \cos \theta} \right)^{-1/2} \quad [23]$$

The minimum finger width ( $v' = 0$ ) predicted by Eq. [23] is independent of aperture and similar to that obtained from Eq. [9] at  $U = 0$ . However, Eq. [23] applies for finite amplitude fingers with a local fluid velocity,  $v'$ , and contains a different leading factor; that is, 2 vs.  $\pi(3)^{0.5}$  in Eq. [9]. Next, in the absence of  $r_2$  ( $C/\delta$  small), Eq. [22] simplifies to

$$W = \left( \frac{2\sigma[(r_1^{-1})_{\text{apex}} - (r_1^{-1})_{\text{side}}]}{\Delta \rho g \cos \theta} \right) \left( 1 - \frac{v'}{K_s k_r \cos \theta} \right)^{-1} \quad [24]$$

Here, the minimum finger width will be controlled by the range of apertures sampled at the apex and sides of the finger, respectively. Although the maximum difference between  $(r_1^{-1})_{\text{apex}}$  and  $(r_1^{-1})_{\text{side}}$  will be given by the aperture distribution, the range of apertures sampled will be less, especially in our field where large and small apertures are each spatially correlated with themselves (Fig. 4d).

In our fracture, both  $r_1$  and  $r_2$  curvatures were important ( $C/\delta \approx 1$ ), so behavior will lie somewhere between the extremes presented by Eq. [23] and [24]. Scaled finger width ( $W \cos \theta$ ) is plotted as a function of scaled fingertip velocity ( $v^*$ ) as Fig. 31a; an expanded vertical scale is shown as Fig. 31b. Data obtained under dry initial conditions in both the redistribution and point source experiments plot on a single curve. The Hele-Shaw prediction, Eq. [23], is dependent on both  $v^*$  and  $\cos \theta$ ;  $\cos \theta = 1.0$  proves the best fit, but still underpredicts finger width. The discrepancy increases with  $v^*$ . To plot Eq. [24], we took the range of apertures sampled

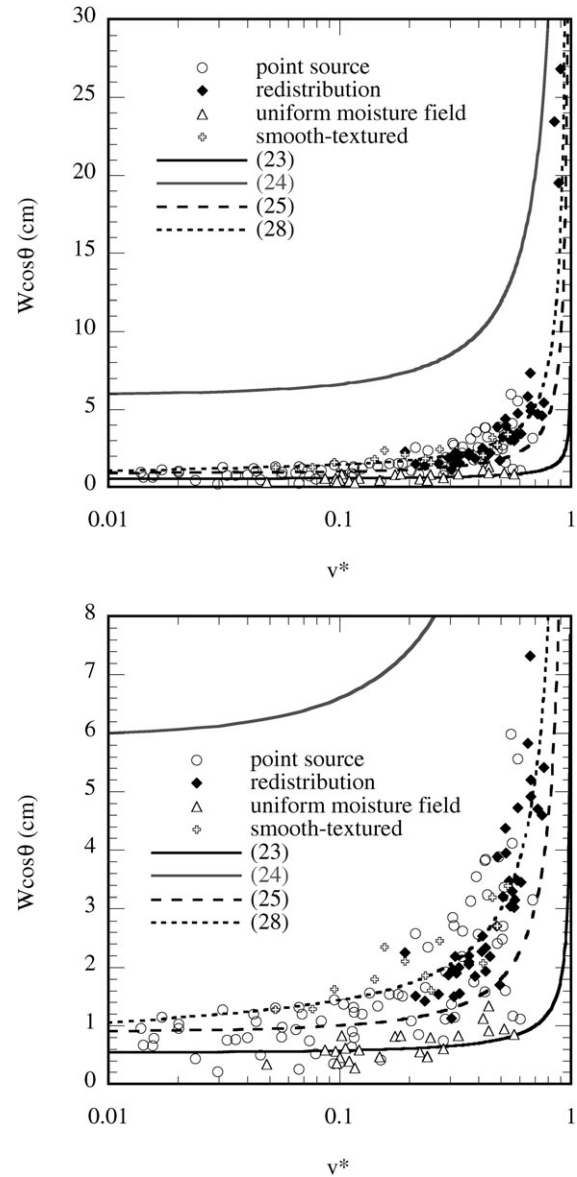


**Fig. 31. Scaled finger width ( $W \cos \theta$ ) is shown as a function of scaled fingertip velocity ( $v^* = v/K_s k_r \cos \theta$ ). Data are shown from the redistribution and point source experiments under dry initial conditions and point source experiments with a uniform initial moisture field. Data are also shown for point source experiments in the smooth-textured aperture field. Lines represent Eq. [23], [24], [25], and [28]. (upper) Full data set. (lower) Range of the y axis ( $W \cos \theta$ ) is reduced to show more detail at small  $W \cos \theta$ .**

to be reflected by the standard deviation,  $\gamma$ , so that  $(r_1^{-1})_{\text{apex}} = \langle a \rangle + \gamma$  and  $(r_1^{-1})_{\text{side}} = \langle a \rangle - \gamma$ . The result vastly overpredicts measured finger widths at small  $v^*$ ; however, the functional form resembles the data more closely than observed for Eq. [23]. To test this hypothesis, we fitted Eq. [24] to our data with the following equation:

$$W \cos \theta = C_0 (1 - v^*)^{-1} \quad [25]$$

where  $C_0$  is an arbitrary constant chosen to fit the data at small  $v^*$  ( $C_0 = 0.9$  cm). This curve fits the data well at the extremes of  $v^*$ , but underpredicts at intermediate to high values of  $v^*$ .

Before continuing, we must point out that the above analysis holds only for dry initial conditions. Experiments in uniformly distributed initial moisture fields suggest that the size, shape, and spatial arrangement of disconnected fluid blobs within the fracture place a first-order control on finger behavior. In general, fingers were observed to be narrower and faster than under dry initial conditions. Measured data for finger width obtained under steady supply to a fracture containing a uniform initial moisture field plot on a separate curve below data obtained under dry initial conditions (Fig. 31a and 31b).

### Dynamic Capillary Pressures

The relations developed above for fingertip length and finger width implicitly assume that capillary pressure will be independent of velocity. However, there is substantial experimental evidence to the contrary (e.g., Hoffman, 1975; de Gennes, 1985; Weitz et al., 1987; Dragila and Weisbrod, 2003). Weitz et al. (1987) measured capillary pressure as a function of interfacial velocity during rectilinear displacement in a porous media that was fabricated from glass beads. They observed that capillary pressure increased from a static value of  $P_0$  according to the following empirical relationship (Weitz et al., 1987):

$$P_c = P_0[1 + \Gamma C_a^n] \quad [26]$$

where  $C_a$  is the capillary number, and  $\Gamma$  and  $n$  are arbitrary constants.  $P_0$  was defined as the maximum pressure at which the interface remained pinned. In experiments with two different sizes of glass beads they estimated  $n \approx 0.5$  and  $\Gamma \approx 300$ .

Looking at Eq. [20], fingertip length will be dependent on pressures along the leading and trailing edges of the finger. For simplicity, we ignore the effects of  $r_2$  curvature and assume that dynamic capillary pressure is mostly dependent on contact angle. The static contact angle for drainage along the trailing edge of the finger will be near zero, and thus experience little change under dynamic conditions. Conversely, contact angle at the fingertip may increase substantially from the static value of 30 to 55°. Following Eq. [26], we rewrite Eq. [20] as

$$L_{\text{tip}} \cos \theta = \frac{\psi_w[1 - (v^*)^n] - \psi_d}{1 - v^*} \quad [27]$$

Using our measured values for  $\psi_w$  and  $\psi_d$  (−2.25 and −5.1 cm, respectively), we found  $n = 0.1$  to provide an excellent fit to our measured data (Fig. 30). The vastly improved fit over Eq. [20] strongly suggests that velocity is an important consideration in the wetting pressure acting along the fingertip. This observation is consistent with recent results by Dragila and Weisbrod (2003), who concluded that dynamic contact angle had a substantial influence on the velocity of discrete droplets in a large aperture ( $\approx 1.7$  mm) fracture with nearly smooth walls.

Prediction of finger width with Eq. [22] requires an estimate for the maximum and minimum capillary pressures along the fingertip. As both of these measures

may differ substantially from  $\psi_w$ , we instead rewrite Eq. [22] with arbitrary fitting parameters ( $C_1$ ,  $C_2$ ) as follows:

$$W \cos \theta = \frac{C_1[1 - (v^*)^n] - C_2}{1 - v^*} \quad [28]$$

Taking  $n = 0.1$ , as above, we fitted Eq. [28] to our data, obtaining estimates for  $C_1$  and  $C_2$  of −1.5 and −1.6 cm, respectively. As seen in Fig. 31a and Fig. 31b, modification of the wetting pressure to include a dependency on velocity improves our estimate over Eq. [24], particularly at intermediate  $v^*$ . While the improvement is not as dramatic as observed for fingertip length (Fig. 30), it does reinforce the importance of dynamic capillary pressure in determining finger width. Note that our choices for  $C_1$  and  $C_2$  are not valid outside the range of our data and in fact lead to an overly low prediction of  $W = 0.1$  cm at  $v^* = 0$ . DiCarlo and Blunt (2000) developed an approximation for the width of constant velocity fingers in homogenous porous media that also includes dynamic capillary pressure. Their result is similar in form to Eq. [28] and also becomes unphysical as finger velocity goes to zero.

## EXPERIMENTAL OBSERVATIONS: EXTENSIONS OF OUR RESULTS

Here, we extend our principal results with a set of illustrative experiments designed to guide future investigations. First, we consider a simple modification to our analog fracture that increases the influence of capillary forces. Next, the addition of micro-roughness to the fracture surfaces introduces film flow along the fracture walls. The effects of aperture variability at the scale of individual fingers or larger are discussed using results from previous experiments. Then we demonstrate that gravity-driven fingers will form despite imbibition by an adjacent matrix. Finally, we conclude with an experiment that considers buoyant nonwetting fingers formed during the upward displacement of water by air.

### Increase in Capillary Forces

We perturbed the balance between capillary, gravity, and viscous forces by replacing one of the textured plates in our 15- by 30-cm analog fracture with a smooth plate (Fig. 4a), thus decreasing  $\langle a \rangle$  and increasing  $\delta$  (Fig. 4c; Table 1) without altering  $\lambda$ . This change increases the relative importance of capillary forces with respect to gravity and viscous forces. In addition, the  $r_1$  component of capillarity gains importance with respect to the  $r_2$  component, as  $C/\delta$  declines from 1.03 to 0.434. We performed a small number of experiments at  $\cos \theta = 1$  in this “smooth-textured” aperture field. In each, steady supply was applied to a point source under dry initial conditions. With respect to our primary analog fracture, fingers in the smooth-textured aperture field displayed increased meandering, a much more irregular outline, and some air entrapment within the saturated fingertip (Fig. 32). Observed behavior results from an increase in  $r_1$  capillary roughening relative to  $r_2$  capillary smoothing (e.g., Glass et al., 2003). Despite the in-

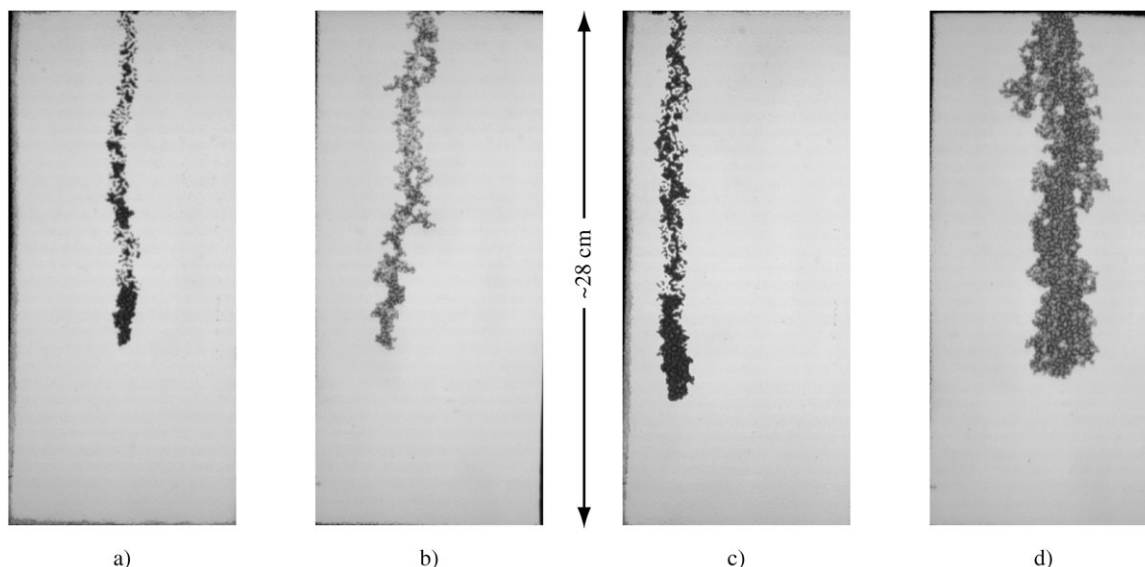


**Fig. 32.** Comparison between (a, c) fingers formed in our primary aperture field and (b, d) the smooth-textured variant. Note that the smaller aperture of the smooth-textured field leads to a lower optical contrast between air and water. (a) Primary aperture field,  $Q = 0.0256 \text{ cm}^3 \text{ min}^{-1}$ . (b) Smooth-textured aperture field,  $Q = 0.0221 \text{ cm}^3 \text{ min}^{-1}$ . (c) Primary aperture field,  $Q = 0.572 \text{ cm}^3 \text{ min}^{-1}$ . (d) Smooth-textured aperture field,  $Q = 0.579 \text{ cm}^3 \text{ min}^{-1}$ .

creased irregularity along the edges of the finger in the smooth-textured aperture field, finger widths were similar between the two analog fractures at low supply rates (Fig. 32a and 32b). This situation changes dramatically as viscous forces come into play with increased supply rate, as finger width becomes much wider in the smooth-textured aperture field (Fig. 32c and 32d). However, when plotted as a function of  $v^*$ , finger widths for the smooth-textured aperture field are similar to data from the primary aperture field (Fig. 31a and 31b). In the smooth-textured aperture field, we also observed more numerous dendrites and tip-splitting bifurcations, a lengthened saturated fingertip, and decreased propensity for intermittent dripping within the desaturated zone.

### Micro-Roughness on the Fracture Surfaces

To consider the influence of aperture micro-roughness on the development of gravity-driven fingers, we sandblasted both textured surfaces of a 15- by 30-cm analog fracture, then applied steady supply from a point source into the air-filled, vertical ( $\cos\theta = 1$ ) cell. The most obvious effect of introducing micro-roughness (and surface cracks of similar scale) was the formation of a film that surrounds the finger and narrows toward the fingertip (Fig. 33a). After finger passage, the film zone continues to grow, becoming of similar width along the entire finger. In Fig. 33b, taken approximately 1 h after flow ceased, we see that the film zone has reached an approximately uniform width and partially drained the stagnant finger structure in the process.

Fingers in the sandblasted fracture took a more tortuous pathway than was observed at similar supply rate in either our primary aperture field (Fig. 32a) or the smooth-textured aperture field (Fig. 32b). Fingers appeared narrower, with increased variability in finger width (Fig. 32a). At a number of locations, width of the

connected saturated zone narrowed to approximately the spatial correlation length of the textured plates ( $\approx 0.08 \text{ cm}$ ). As with the smooth-textured fracture, we noted the fingertip to be considerably longer than observed in our primary aperture field. Combined, these observations suggest that  $C/\delta$  in the sandblasted fractures is slightly less than that for the smooth-textured aperture field, as is the ratio of gravitational to capillary forces. Although we were unable to measure this aperture field, we expect that sandblasting would decrease  $C/\delta$  by reducing  $\langle a \rangle$  and broadening the small end of the aperture distribution (increasing  $\delta$ ).

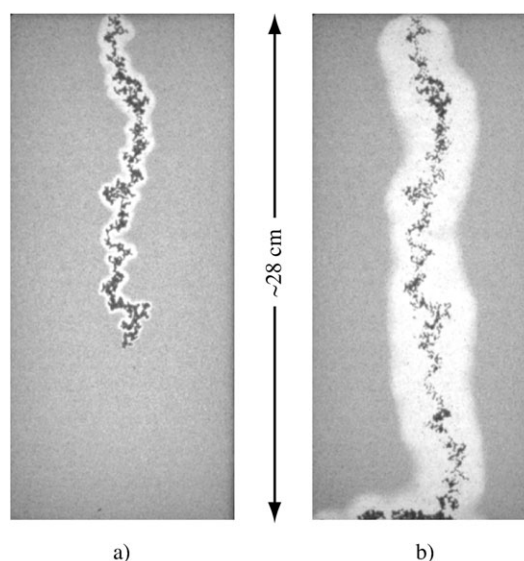


**Fig. 33.** Finger formed under dry initial conditions in the sandblasted aperture field at  $\cos\theta = 1.0$ . Steady supply of  $Q = 0.0236 \text{ cm}^3 \text{ min}^{-1}$  is comparable to that for the images shown in Fig. 32a and 32b. The sandblasted plates diffused a significant amount of light, reducing contrast in the images.



### Natural Fracture Aperture Fields with Larger-Scale Heterogeneity

Aperture variability at scales on the order of finger width and larger is expected to influence gravity-driven fingers. Redistribution of ponded infiltration ( $13 \text{ cm}^3$  of dyed water) into an initially dry natural fracture (Fig. 34) led to the formation of gravity-driven fingers (Nicholl et al., 1994). In comparing Fig. 34 with Fig. 5d, we see both similarities and differences. In both cases, the top of the fracture was fully wetted, which suggests that infiltration was initially stable. The uniformly wetted area extends to greater depth in Fig. 34, suggesting that  $V_p$  was not small with respect to the aperture volume (see also Fig. 6). Below the uniformly wetted region, both experiments (Fig. 5d and 34) showed the development of multiple gravity-driven fingers. Within each experiment, finger width appears to be relatively uniform across all fingers, and along individual fingers. Finger outlines are fairly smooth in both experiments, suggesting a strong  $r_2$  influence (Fig. 32). The clear definition of finger edges in both experiments suggests a lack of substantial film flow in the fracture (Fig. 33).

Fingers seen in Fig. 34 differ from observations in our primary analog at  $\cos\theta = 1$  (Fig. 5d) in that they tend to meander more about the fracture surface and occasionally merge with one another. From our other experiments (Fig. 13), we see that fingers meander when the importance of capillary forces is increased with respect to gravitational forces. In aperture fields where fingers are larger than the aperture spatial correlation length (such as our analog fractures), finger location will depend on the boundary and initial conditions. Aperture variability will provide a mostly local influence

that increases as both  $C/\delta$  and the ratio of gravity to capillary forces decreases (increased inclination, or decreased mean aperture). In Fig. 34, the characteristic length scale and degree of heterogeneity present is sufficient to modify finger behavior, but not to completely control (channel) the displacement process. Where the aperture heterogeneity is sufficiently extreme, it will constrain the location of fingers to specific channels. Such channeling was demonstrated by Su et al. (1999) with cast epoxy replicas of natural fractures.

### Matrix Imbibition

Fluid exchange between the fractures and the adjacent porous media is expected for most fractured rock systems (e.g., Nativ et al., 1995; Robinson and Bussod, 2000; Glass et al., 2002b; Faybishenko et al., 2000, 2003; Su et al., 2003). If the fracture surfaces and porous media have similar surface chemistry (i.e., wettability), the main difference between the two will be that apertures in the fracture are expected to be relatively large and connected in two dimensions, while the adjacent porous media will be characterized by much smaller pores connected in a three-dimensional network. If the porous media is at or near saturation, water may move onto the rough fracture surfaces and flow as film (e.g., Tokunaga and Wan, 1997; Or and Tuller, 2000). Conversely, capillary forces will act to draw water from a flowing fracture into an adjacent, unsaturated matrix. However, fracture flow is expected wherever fluid supplied to the fracture exceeds the local imbibition capacity of the matrix. The experiment shown in Fig. 34 is an end member case where the porous media is of low porosity and conductivity and has little effect on displacement in the fracture or the formation of gravity-driven fingers. The same would be expected when a porous matrix of any porosity and conductivity is water-saturated and thus has little or no absorption capacity.

When water is supplied to a fracture at a rate just above the imbibition capacity of the matrix, fluid will be drawn into the matrix, modifying or possibly suppressing the growth of gravity-driven fingers. Glass and Tidwell (1991) fabricated a vertical analog fracture in which a saw-cut slab (0.6 by 0.6 m) of welded tuff was secured to a textured glass plate. Both the rock slab and the fracture were initially dry. Steady supply to a point source along the upper boundary led to the formation of a gravity-driven finger within the fracture, despite obvious imbibition into the adjacent matrix (Fig. 35). The finger meandered significantly and exhibited a highly variable width. At later time it formed a dendrite that connected back to the primary finger (Fig. 35c). The wetted zone within the matrix surrounding the advancing fingertip was similar to that seen in Fig. 33a, where micro-roughness caused film flow away from the growing finger. Gravity-driven fingering within the fracture limits hydraulic communication between fluid in the fracture and the matrix. As a result, imbibition capacity is satisfied locally, and the matrix is unable to draw off sufficient fluid to suppress finger formation. Note that the complexity and limited extent of the wet-

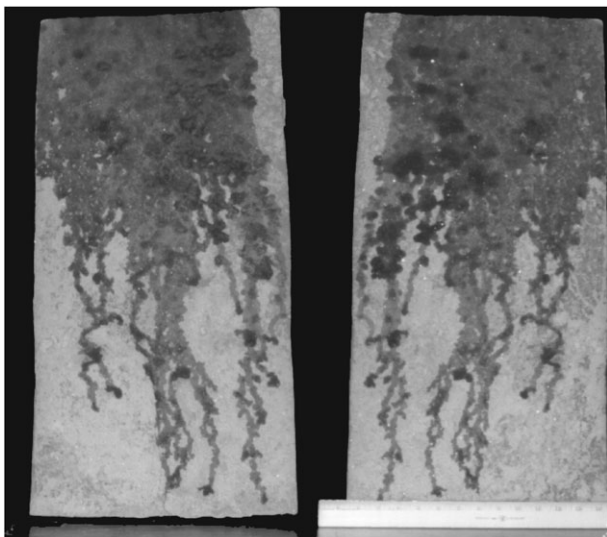


Fig. 34. Ponded infiltration ( $V_p = 13 \text{ cm}^3$ ) into a 32- by 66-cm natural fracture at  $\cos\theta = 1.0$ . Dye stains (dark) show a transition from stable infiltration to gravity-driven fingers. Unlike our analog, the natural fracture does not allow us to observe the development of fingers, only the end result following disassembly. Because the dye permanently stains the rock, internal flow structure is obscured and we can only see the area wetted by infiltration. The fracture was collected from an outcrop of densely welded volcanic ash located near Los Alamos, NM (from Nicholl et al., 1994).

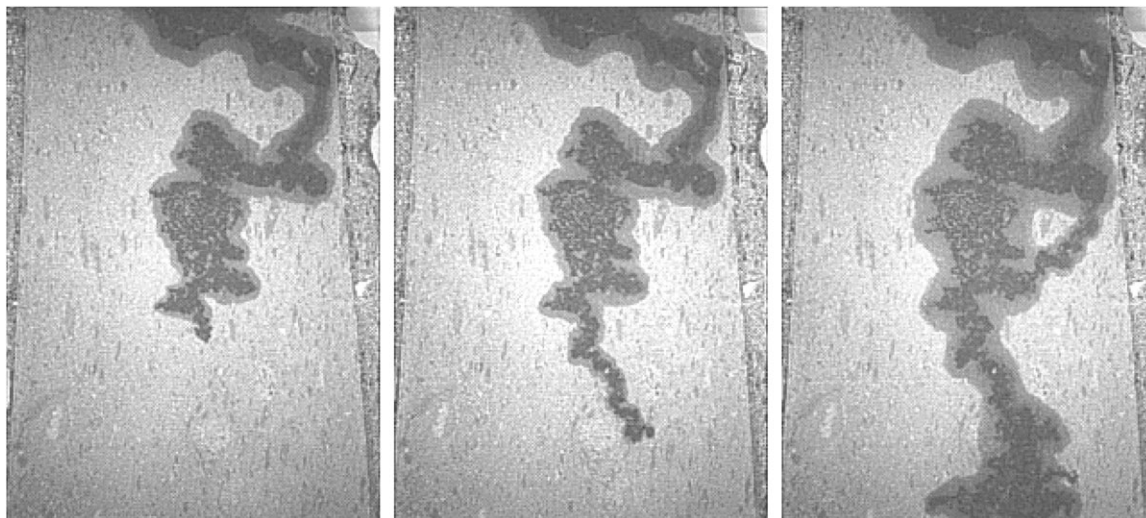


Fig. 35. Development of a gravity-driven finger in an analog fracture-matrix system. The darkest zones mark a gravity-driven finger moving downward through the fracture. The somewhat lighter fringe shows matrix wetting (from Glass and Tidwell, 1991).

ted area ( $\approx 15\%$  of the fracture plane) have important implications both for the fracture-matrix interaction and flow across the fracture plane between adjacent matrix blocks (e.g., Glass et al., 1995).

### Buoyant Nonwetting Fingers

We performed a single experiment in which water was displaced during upward invasion by air (Fig. 36). From Eq. [6], this scenario is fundamentally unstable (upward displacement by a less viscous, less dense fluid) and is directly relevant to tunnel design in water saturated rock (Glass and Nicholl, 1995). We saturated the 15- by 30-cm analog fracture, sealed three edges (top and both sides), and held it vertically ( $\cos\theta = 1$ ). We then slowly moved dry air along the unsealed bottom boundary. Subsequent evaporation led to upward invasion by the nonwetting air phase. Figure 36a is a compos-

ite image showing the regions swept by rising air fingers (in black). Two “tracks” formed, one along the right-hand edge of the system and another within the aperture field on the left. Contrary to results for wetting fingers, rising air fingers did not readily connect with remnants of previous fingers pinned within the fracture. Thus, the “envelope” of the rising finger widened with time and distance from the evaporative surface.

The growth of a single air finger is illustrated in Fig. 36b through 36d, a three-image sequence that focuses in on the boxed region of Fig. 36a. The air finger grows first horizontally, then upward. The fingertip moves upward as a unit when it reaches sufficient length for buoyancy to overcome capillary forces. Water reinvades behind the fingertip, which fragments to leave a trail of entrapped air blobs. The finger shows a highly variable width, with narrow necks and wider zones that entrap

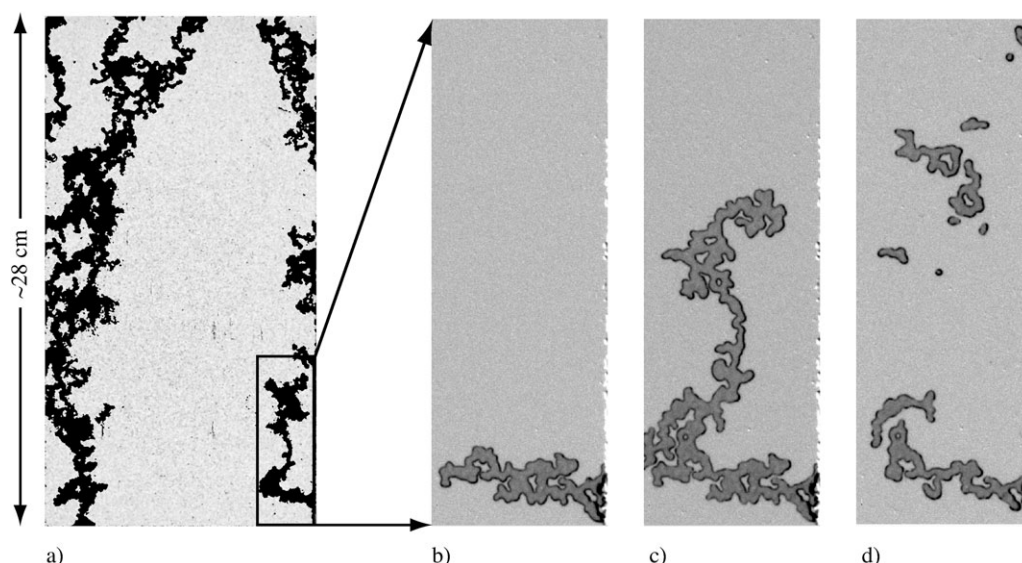


Fig. 36. Buoyant air invasion into a 15- by 30-cm vertical analog fracture saturated with deionized water. (a) Portions of the analog fracture swept by rising air bubbles are shown in black, while the speckled gray zones remained water saturated (from Glass and Nicholl, 1995). (b–d) This sequence shows the growth and fragmentation of an air finger within the boxed region of (a).



the displaced water phase. This increased complication over wetting displacement in the same fracture reflects a decrease in  $C/\delta$  for nonwetting invasion. From Eq. [5] the magnitude of  $r_1$ -related capillary forces are inversely proportional to  $\cos\alpha$ , which will be at a maximum for nonwetting displacement; that is,  $\alpha \approx 180^\circ$ , rather than  $35$  to  $55^\circ$  for displacement by water. Thus, for the surface chemistry of our system,  $C$  for wetting displacement will be greater than for nonwetting. Complication is additionally enhanced for nonwetting invasion due to the increase in the effective  $\delta$  operational during nonwetting invasion.

## CONCLUSIONS

As a step toward understanding flow in unsaturated fractured rock we studied the formation and behavior of gravity-driven fingers during infiltration into individual fractures. We found gravity-driven fingers to occur across a wide range of fluid-supply conditions, initial moisture contents, and in near-horizontal fractures. This widespread occurrence emphasizes their importance to flow and transport in unsaturated fractured rock. Fingers will move much faster and further than would be expected for an equivalent uniform infiltration front. Fingering flow also restricts contact with the adjacent porous matrix, thus limiting the influence of the matrix to retard or mitigate contaminant migration.

With respect to the processes that control gravity-driven fingering within individual fractures, our investigations led to a number of key results. Fingers formed during the redistribution of ponded infiltration exhibited a first-order dependency on finite amplitude perturbations present before fragmentation of the fluid slug. Fingers formed from steady supply to a point source showed substantial desaturation behind the fingertip at large  $\cos\theta$  and small supply rates, with fingertips disconnecting completely from the fluid source. The desaturated zone could exhibit significant dynamics, leading to formation of dendritic secondary fingers and intermittent flow structures. When the fracture was prewetted by previous unstable events, fingers exhibited a persistent spatial structure similar to that observed in porous media. However, in a result contrary to the porous media literature, we observed increased instability within uniformly distributed initial moisture fields. The mechanism for the increased instability was the dichotomous nature of initial moisture in our analog fracture, in which local saturation was either 0 or 100%. Fully saturated fluid blobs acted as instantaneous perturbations to advancing fingertips, increasing instability. Finally, a simple scale analysis produced predictive models for finger width and length as functions of finger velocity. For both parameters, data across different experiments, boundary conditions, and  $\cos\theta$  collapsed to single curves. In fitting our models, it was necessary to account for the effects of velocity on capillary pressure at the fingertip, which we assumed to be primarily a function of dynamic contact angle.

Additional experiments designed to extend our primary results suggest that gravity-driven fingers will

readily form during infiltration into natural rock units. In separate experiments, fingers were observed to form in heterogeneous aperture fields, in the presence of micro-roughness, and adjacent to a dry porous matrix. While the full spectrum of parameter space remains to be explored, these results suggest that gravity-driven fingers are robust features at the scale of single fractures. At the network-scale, fracture intersections are expected to impose a capillary heterogeneity that would integrate gravity-driven fingers (Glass et al., 1995; Wood et al., 2002) and possibly lead to large-scale confluencing. Such confluencing has been recently reported in a set of simple experiments where a fracture network is formed within a regular array of porous blocks (LaViolette et al., 2003). Pulsation along gravity-driven fingers within individual fractures is believed to be mostly responsible for the high-frequency component of the outflow signal from a fracture-matrix network, with the lower-frequency component resulting from network-scale processes (Glass et al., 2002a).

Another of our extensions considered upward migration of air in a water filled fracture. The less dense, nonwetting air phase formed irregular fingers that fragmented to form a complicated two-phase structure within the analog fracture. While this situation has direct relevance for the creation of an unsaturated zone surrounding a tunnel emplaced below the water table, it is also analogous to the density-driven migration of DNAPLs. Given their relative density, DNAPLs will migrate downward as the displacing fluid in both the unsaturated and saturated zones. Because DNAPLs are nonwetting to most geologic media, fractures are expected to act as preferential conduits. Thus, inverting Fig. 36 gives one an idea of the potential complexity associated with the location, characterization, and remediation of DNAPLs in fractured bedrock. This is an open and important area of research that has received little attention.

## APPENDIX

### Notation

$a$	local fracture aperture (L)
$\langle a \rangle$	mean of the aperture field (L)
$A, B$	arbitrary locations along an air-water interface
$C$	curvature number (dimensionless)
$C_0$	arbitrary constant (L)
$C_1$	arbitrary constant (L)
$C_2$	arbitrary constant (L)
$C_a$	capillary number (dimensionless)
$g$	gravitational constant ( $L T^{-2}$ )
$h_g$	gravitational length scale (L)
$h_v$	viscous length scale (L)
$k$	intrinsic permeability ( $L^2$ )
$k_r$	relative permeability (dimensionless)
$K_s$	saturated hydraulic conductivity ( $L T^{-1}$ )
$L_{tip}$	saturated fingertip length (L)
$L_i$	infiltration length (L)
$n$	arbitrary constant (dimensionless)
$P_c$	capillary pressure jump ( $F L^{-2}$ )
$P_o$	maximum static capillary pressure jump ( $F L^{-2}$ )
$\Delta P_c$	local pressure differential associated with capillary forces ( $F L^{-2}$ )



$\Delta P_g$	local pressure differential associated with gravitational forces ( $F L^{-2}$ )
$\Delta P_v$	local pressure differential associated with viscous forces ( $F L^{-2}$ )
$q$	fluid flux ( $L T^{-1}$ )
$Q$	fluid supply rate ( $L^3 T^{-1}$ )
$r_1$	first principal radius of interfacial curvature (L)
$r_2$	second principal radius of interfacial curvature (L)
Re	Reynolds number (dimensionless)
$t$	time after starting an experiment (T)
$U$	interfacial velocity ( $L T^{-1}$ )
$v$	fingertip velocity ( $L T^{-1}$ )
$v^*$	scaled fingertip velocity (dimensionless)
$v'$	local fluid velocity ( $L T^{-1}$ )
$V_p$	volume of water added to the pond ( $L^3$ )
$W$	finger width (L)
$\alpha$	fluid–fluid–solid contact angle
$\beta$	angle of local aperture convergence–divergence
$\delta$	coefficient of variation for the aperture field ( $L L^{-1}$ )
$\phi$	included angle used to parameterize interfacial curvature
$\gamma$	standard deviation of the aperture field (L)
$\lambda$	aperture spatial correlation length (L)
$\lambda_m$	fastest growing wavelength (L)
$\psi_w$	wetting pressure head (L)
$\psi_d$	drainage pressure head (L)
$\mu$	kinematic viscosity ( $M L^{-1} T^{-3}$ )
$\rho$	fluid density ( $M L^{-3}$ )
$\sigma$	interfacial tension ( $M T^{-2}$ )
$\theta$	included angle between vertical downward and the fracture plane
$\Gamma$	arbitrary constant (dimensionless)

## ACKNOWLEDGMENTS

Experiments were conducted in the Flow Visualization and Processes Laboratory at Sandia National Laboratories over an approximately 10 year period beginning in 1989. From 1989 to 1996, support was provided by the U.S. Department of Energy, Office of Civilian Radioactive Waste Management, Yucca Mountain Site Characterization Project Office, under contract DE-AC04-76DP00789. Original data from that time period are contained in Sandia National Laboratories Yucca Mountain Project controlled scientific notebooks as part of the L19-1/15/90 data set. Subsequent to 1996, this work was continued with support from the U.S. Department of Energy, Basic Energy Sciences Geoscience Research Program under contract numbers DE-FG03-01ER15122 (M.J. Nicholl) and DE-AC04-94AL85000 (R.J. Glass). We gratefully acknowledge that support, which has allowed us to evaluate and interpret data for preparation of this manuscript. M.J. Nicholl received additional support from the U.S. Department of Energy, Environmental Management Science Program under contract DE-FG07-02ER63499. We would also like to thank Craig Ginn, David Lopez, Huy Nguyen, Lee Orear, and Vince Tidwell for their aid in constructing and performing the experiments. Finally, we would like to thank the anonymous reviewers whose input greatly improved this manuscript.

## REFERENCES

- Benson, D.A. 2001. A model of water streaking down a wall. *Water Resour. Res.* 37:427–430.
- Brown, S.R. 1989. Transport of fluid and electric current through a single fracture. *J. Geophys. Res.* 94(B7):9429–9438.
- Brown, S.R. 1995. Simple mathematical model of a rough fracture. *J. Geophys. Res.* 100(B4):5941–5952.
- Brown, S.R., and C.H. Scholz. 1985. Broad bandwidth study of the topography of natural rock surfaces. *J. Geophys. Res.* 90(B14):12,575–12,582.
- Chen, G.L., and S.P. Neuman. 1996. Wetting front instability in randomly stratified soils. *Phys. Fluids*. 8:353–369.
- Chen, G., M. Taniguchi, and S.P. Neuman. 1995. Overview of instability and fingering during immiscible fluid flow in porous and fractured media. Rep. NUREG/CR 6308. Nuclear Regulatory Commission, Washington, DC.
- Chouke, R.L., P. van Meurs, and C. van der Poel. 1959. The instability of slow immiscible, viscous liquid-liquid displacements in porous media. *Trans. AIME* 216:8073, 188–194.
- de Gennes, P.G. 1985. Wetting: Statics and dynamics. *Rev. Modern Phys.* 57:827–863.
- de Rooij, G.H. 2000. Modeling fingered flow of water in soils owing to wetting front instability: A review. *J. Hydrol. (Amsterdam)* 231:277–294.
- Detwiler, R.L., S.E. Pringle, and R.J. Glass. 1999. Measurement of fracture aperture fields using transmitted light: An evaluation of measurement errors and their influence on simulations of flow and transport through a single fracture. *Water Resour. Res.* 35:2605–2617.
- DiCarlo, D.A., and M.J. Blunt. 2000. Determination of finger shape using the dynamic capillary pressure. *Water Resour. Res.* 36:2781–2785.
- Diment, G.A., and K.K. Watson. 1985. Stability analysis of water movement in unsaturated porous materials. 3. Experimental studies. *Water Resour. Res.* 21:979–984.
- Dragila, M.I., and N. Weisbrod. 2003. Parameters affecting maximum fluid transport in large aperture fractures. *Adv. Water Resour.* 26:1219–1228.
- Durham, W.B., W.L. Bourcier, and E.A. Burton. 2001. Direct observation of reactive flow in a single fracture. *Water Resour. Res.* 37:1–12.
- Dussan, V. 1979. On the spreading of liquids on solid surfaces: Static and dynamic contact lines. *Ann. Rev. Fluid Mech.* 11:371–400.
- Eliassi, M., and R.J. Glass. 2002. On the porous continuum-scale simulation of gravity-driven fingers in unsaturated materials: Extension of standard theory with a hold-back-pile-up effect. *Water Resources Res.* 38(11):1234. doi:10.1029/2001WR001131.
- Faybishenko, B., C. Doughty, S. Steiger, J. Long, T. Wood, J. Jacobsen, J. Lore, and P. Zawislanski. 2000. Conceptual model of the geometry and physics of water flow in a fractured basalt vadose zone. *Water Resour. Res.* 36:3499–3520.
- Faybishenko, B., G.S. Bodvarsson, and R. Salve. 2003. On the physics of unstable infiltration, seepage, and gravity drainage in partially saturated tuffs. *J. Contam. Hydrol.* 62–63:63–87, 2003.
- Fourar, M., S. Bories, R. Lenormand, and P. Persoff. 1993. Two-phase flow in smooth and rough fractures: Measurement and correlation by porous-medium and pipe flow models. *Water Resour. Res.* 29:3699–3708.
- Glass, R.J., and M.J. Nicholl. 1995. Near drift two-phase flow processes within regionally saturated fractured rock. p. 212–213. *In* Proc. Sixth Annual International Conference on High Level Radioactive Waste Management. 1–5 May 1995. American Nuclear Society, Las Vegas, NV.
- Glass, R.J., and M.J. Nicholl. 1996. Physics of gravity-driven fingering of immiscible fluids within porous media: An overview of current understanding and selected complicating factors. *Geoderma* 70:133–163.
- Glass, R.J., M.J. Nicholl, S.E. Pringle, and T.R. Wood. 2002a. Unsaturated flow through a fracture-matrix network: Dynamic preferential pathways in meso-scale laboratory experiments. *Water Resour. Res.* 38(12):1281. doi:10.1029/2001WR001002.
- Glass, R.J., M.J. Nicholl, A.L. Ramirez, and W.D. Daily. 2002b. Liquid phase structure within an unsaturated fracture network beneath a surface infiltration event: Field experiment. *Water Resour. Res.* 38(10):1199. doi:10.1029/2000wr000167.
- Glass, R.J., M.J. Nicholl, and V.C. Tidwell. 1995. Challenging models for flow in unsaturated, fractured rock through exploration of small scale flow processes. *Geophys. Res. Lett.* 22:1457–1460.
- Glass, R.J., M.J. Nicholl, and L. Yarrington. 1998. A modified invasion percolation model for low capillary number immiscible displacements in horizontal rough walled fractures: Influence of local in-plane curvature. *Water Resour. Res.* 34:3215–3234.
- Glass, R.J., J.-Y. Parlange, and T.S. Steenhuis. 1989a. Wetting front instability. I. Theoretical discussion and dimensional analysis. *Water Resour. Res.* 25:1187–1194.

- Glass, R.J., H. Rajaram, and R.L. Detwiler. 2003. Immiscible displacements in rough-walled fractures: Competition between roughening by random aperture variations and smoothing by in-plane curvature. *Phys. Rev. E* 68(6):061110. doi:10.1103/PhysRevE.68.061110.
- Glass, R.J., T.S. Steenhuis, and J.-Y. Parlange. 1988. Wetting front instability as a rapid and far-reaching hydrologic process in the vadose zone. *J. Contam. Hydrol.* 3:207–226.
- Glass, R.J., T.S. Steenhuis, and J.-Y. Parlange. 1989b. Wetting front instability. II. Experimental determination of relationships between system parameters and two-dimensional unstable flow field behavior in initially dry porous media. *Water Resour. Res.* 25:1195–1207.
- Glass, R.J., T.S. Steenhuis, and J.-Y. Parlange. 1989c. Mechanism for finger persistence in homogeneous unsaturated porous media: Theory and verification. *Soil Sci.* 48:60–70.
- Glass, R.J., and V.C. Tidwell. 1991. Research program to develop and validate conceptual models for flow and transport through unsaturated, fractured rock. p. 977–987. *In Proc. Second Annual International Conference on High Level Radioactive Waste Management.* 28 Apr.–3 May 1991. American Nuclear Society, Las Vegas, NV.
- Hakami, E., and E. Larsson. 1996. Aperture measurements and flow experiments on a single natural fracture. *Int. J. Rock Mech. Miner. Sci. Geomech. Abstr.* 33:395–404.
- Hanna, R.B., and H. Rajaram. 1998. Influence of aperture variability on dissolutional growth of fissures in karst formations. *Water Resour. Res.* 34:2843–2853.
- Hill, D.E., and J.-Y. Parlange. 1972. Wetting front instability in layered soils. *Soil Sci. Soc. Am. Proc.* 36:697–702.
- Hoffman, R.L. 1975. A study of the advancing interface. Part 1. Interface shape in liquid-gas systems. *J. Colloid Interface Sci.* 50:228–241.
- Homsy, G.M. 1987. Viscous fingering in porous media. *Ann. Rev. Fluid Mech.* 19:271–311.
- Johns, R.A., J.S. Steude, L.M. Castanier, and B.V. Roberts. 1993. Nondestructive measurements of fracture aperture in crystalline rock cores using X-ray computed tomography. *J. Geophys. Res.* 98(B2):1889–1900.
- Jury, W.A., Z. Wang, and A. Tuli. 2003. A conceptual model of unstable flow in unsaturated soil during redistribution. Available at [www.vadosezonejournal.org](http://www.vadosezonejournal.org). *Vadose Zone J.* 2:61–67.
- Keller, A. 1998. High resolution, non-destructive measurement and characterization of fracture apertures. *Int. J. Rock Mech. Miner. Sci.* 35:1037–1050.
- LaViolette, R.A., R.J. Glass, T.R. Wood, T.R. McJunkin, K.S. Noah, R.K. Podgorney, R.C. Starr, and D.L. Stoner. 2003. Convergent flow observed in a laboratory-scale unsaturated fractured system. *Geophys. Res. Lett.* 30(2):1083. doi:10.1029/2002GL015775.
- Lee, J., J.M. Kang, and J. Choe. 2003. Experimental analysis on the effects of variable apertures on tracer transport. *Water Resour. Res.* 39(1):1015. doi:10.1029/2001WR001246.
- Liu, Y.P., T.S. Steenhuis, and J.Y. Parlange. 1994. Formation and persistence of fingered flow-fields in coarse-grained soils under different moisture contents. *J. Hydrol. (Amsterdam)* 159(1–4):187–195.
- Murphy, J.R., and N.R. Thomson. 1993. Two-phase flow in a variable aperture fracture. *Water Resour. Res.* 29:3453–3476.
- National Research Council. 1996. *Rock fractures and fluid flow: Contemporary understanding and application.* National Academy Press, Washington, DC.
- Nativ, R., E. Adar, O. Dahan, and M. Geyh. 1995. Water recharge and solute transport through the vadose zone of fractured chalk under desert conditions. *Water Resour. Res.* 31:253–261.
- Nicholl, M.J., R.J. Glass, and H.A. Nguyen. 1992. Gravity-driven fingering in unsaturated fractures. p. 321–331. *In Proc. Third Annual International Conference on High Level Radioactive Waste Management.* 12–16 Apr. 1992. American Nuclear Society, Las Vegas, NV.
- Nicholl, M.J., R.J. Glass, and H.A. Nguyen. 1993a. Small-scale behavior of single gravity-driven fingers in an initially dry fracture. p. 2023–2032. *In Proc. Fourth Annual International Conference on High Level Radioactive Waste Management.* 26–30 Apr. 1993. American Nuclear Society, Las Vegas, NV.
- Nicholl, M.J., R.J. Glass, and H.A. Nguyen. 1993b. Wetting front instability in an initially wet unsaturated fracture. p. 2061–2070. *In Proc. Fourth Annual International Conference on High Level Radioactive Waste Management.* 26–30 Apr. 1993. American Nuclear Society, Las Vegas, NV.
- Nicholl, M.J., R.J. Glass, and S.W. Wheatcraft. 1994. Gravity-driven infiltration instability in initially dry nonhorizontal fractures. *Water Resour. Res.* 30:2533–2546.
- Nicholl, M.J., H. Rajaram, and R.J. Glass. 2000. Factors controlling saturated relative permeability in a partially-saturated horizontal fracture. *Geophys. Res. Lett.* 27:393–396.
- Nicholl, M.J., H. Rajaram, R.J. Glass, and R. Detwiler. 1999. Saturated flow in a single fracture: Evaluation of the Reynolds equation in measured aperture fields. *Water Resour. Res.* 35:3361–3373.
- Or, D., and M. Tuller. 2000. Flow in unsaturated fractured porous media: Hydraulic conductivity of rough surfaces. *Water Resour. Res.* 36:1165–1178.
- Parlange, J.-Y., and D.E. Hill. 1976. Theoretical analysis of wetting front instability in soils. *Soil Sci.* 122:236–239.
- Persoff, P., and K. Pruess. 1995. Two-phase flow visualization and relative permeability measurement in rough-walled fractures. *Water Resour. Res.* 31:1175–1186.
- Philip, J.R. 1975. Stability analysis of infiltration. *Soil Sci. Soc. Am. Proc.* 39:1042–1049.
- Plouraboue, F., P. Kurowski, J.-P. Hulin, S. Roux, and J. Schmittbuhl. 1995. Aperture of rough cracks. *Phys. Rev. E* 51:1675–1685.
- Poon, C.Y., R.S. Sayles, and T.A. Jones. 1992. Surface measurement and fractal characterization of naturally fractured rocks. *J. Phys. D: Appl. Phys.* 25:1269–1275.
- Raats, P.A.C. 1973. Unstable wetting fronts in uniform and non-uniform soils. *Soil Sci. Soc. Am. Proc.* 37:681–685.
- Robinson, B.A., and G.Y. Bussod. 2000. Radionuclide transport in the unsaturated zone at Yucca Mountain: Numerical model and preliminary field observations. p. 323–336. *In B. Faybishenko et al. (ed.) Dynamics of fluids in fractured rock.* Geophysical Monogr. 122. AGU, Washington, DC.
- Saffman, P.G. 1986. Viscous fingering in Hele-Shaw cells. *J. Fluid Mech.* 173:73–94.
- Saffman, P.G., and G.I. Taylor. 1958. The penetration of a fluid into a porous medium or Hele-Shaw cell containing a more viscous liquid. *Proc. R. Soc. London A245*:312–331.
- Scanlon, B.R., S.W. Tyler, and P.J. Wierenga. 1997. Hydrologic issues in arid, unsaturated systems and implications for contaminant transport. *Rev. Geophys.* 35:461–490.
- Schaefer, C.J. 2002. Field characterization and thermal-mechanical analysis of fracture distributions in basalt lava flows, Eastern Snake River Plain, Idaho. M.S. thesis. University of Idaho, Moscow, ID.
- Schmittbuhl, J., F. Schmitt, and C.H. Scholz. 1995. Scaling invariance of crack surfaces. *J. Geophys. Res.* 100(B4):5953–5973.
- Selker, J.S., T.S. Steenhuis, and J.Y. Parlange. 1992a. Wetting front instability in homogenous sandy soils under continuous infiltration. *Soil Sci. Soc. Am. J.* 56:1346–1350.
- Selker, J.S., J.Y. Parlange, and T.S. Steenhuis. 1992b. Fingered flow in two dimensions. 2. Predicting finger moisture profile. *Water Resour. Res.* 28:2523–2528.
- Shaw, R. 1984. *The dripping faucet as a model chaotic system.* Aerial Press, Santa Cruz, CA.
- Streit, J.E., and S.F. Cox. 2000. Asperity interaction during creep of simulated faults at hydrothermal conditions. *Geology* 28:231–234.
- Su, G.W., J.T. Geller, J.R. Hunt, and K. Pruess. 2004. Gravity-driven flow in unsaturated fractures. Available at [www.vadosezonejournal.org](http://www.vadosezonejournal.org). *Vadose Zone J.* 3:592–601.
- Su, G.W., J.T. Geller, K. Pruess, and J.R. Hunt. 2001. Solute transport along preferential flow paths in unsaturated fractures. *Water Resour. Res.* 37:2481–2491.
- Su, G.W., J.T. Geller, K. Pruess, and F. Wen. 1999. Experimental studies of water seepage and intermittent flow in unsaturated, rough-walled fractures. *Water Resour. Res.* 35:1019–1037.
- Su, G.W., J.R. Nimmo, and M.I. Dragila. 2003. Effect of isolated fractures on accelerated flow in unsaturated porous rock. *Water Resour. Res.* 39(12):1326. doi:10.1029/2002WR001691.
- Throckmorton, C.K., and E.R. Verbeek. Joint networks in the Tiva Canyon and Topopah Springs tuffs of the Paintbrush Group, southwestern Nevada. USGS Open-File Rep. 95-2. USGS, Denver, Colorado, 1995.

- Tokunaga, T.K., and J. Wan. 1997. Water film flow along fracture surfaces of porous rock. *Water Resour. Res.* 33:1287–1295.
- Wang, Z., W.A. Jury, A. Tuli, and D.-J. Kim. 2004. Unstable flow during redistribution: Controlling factors and practical implications. Available at [www.vadosezonejournal.org](http://www.vadosezonejournal.org). *Vadose Zone J.* 3:549–559.
- Wang, Z., A. Tuli, and W.A. Jury. 2003a. Unstable flow during redistribution in homogenous soil. Available at [www.vadosezonejournal.org](http://www.vadosezonejournal.org). *Vadose Zone J.* 2:52–60.
- Wang, Z., L. Wu, T. Harter, J. Lu, and W.A. Jury. 2003b. A field study of unstable preferential flow during soil water redistribution. *Water Resour. Res.* 39(4):1075. doi:10.1029/2001WR000903.
- Weisbrod, N., R. Nativ, E. Adar, D. Ronen, and A. Ben-Nun. 2000. The impact of coating and weathering on the properties of chalk fracture surfaces. *J. Geophys. Res.* 105(B12):27,853–27,864.
- Weisbrod, N., R. Nativ, D. Ronen, and E. Adar. 1998. On the variability of fracture surfaces in unsaturated chalk. *Water Resour. Res.* 34:1881–1887.
- Weitz, D.A., J.P. Stokes, R.C. Ball, and A.P. Kushnick. 1987. Dynamic capillary pressure in porous media: Origin of the viscous-fingering length scale. *Phys. Rev. Lett.* 59:2967–2970.
- Wood, T.R., M.J. Nicholl, and R.J. Glass. 2002. Fracture intersections as integrators for unsaturated flow. *Geophys. Res. Lett.* 29(24):2191. doi:10.1029/2002GL015551.
- Zimmerman, R.W., and G.S. Bodvarsson. 1996. Hydraulic conductivity of rock fractures. *Transp. Porous Media* 23:1–30.